



**HAL**  
open science

## Comprehensive characterization of sooting butane jet flames, Part 2: Temperature and soot particle size

I.A. Mulla, Jérôme Yon, David Honoré, C. Lacour, A. Cessou, Bertrand Lecordier

### ► To cite this version:

I.A. Mulla, Jérôme Yon, David Honoré, C. Lacour, A. Cessou, et al.. Comprehensive characterization of sooting butane jet flames, Part 2: Temperature and soot particle size. *Combustion and Flame*, In press, pp.111596. 10.1016/j.combustflame.2021.111596 . hal-03351026

**HAL Id: hal-03351026**

**<https://normandie-univ.hal.science/hal-03351026>**

Submitted on 18 Oct 2021

**HAL** is a multi-disciplinary open access archive for the deposit and dissemination of scientific research documents, whether they are published or not. The documents may come from teaching and research institutions in France or abroad, or from public or private research centers.

L'archive ouverte pluridisciplinaire **HAL**, est destinée au dépôt et à la diffusion de documents scientifiques de niveau recherche, publiés ou non, émanant des établissements d'enseignement et de recherche français ou étrangers, des laboratoires publics ou privés.

# Comprehensive characterization of sooting butane jet flames, Part 2: temperature and soot particle size

I.A. Mulla<sup>a,b</sup>, J. Yon<sup>b</sup>, D. Honoré<sup>b</sup>, C. Lacour<sup>b</sup>, A. Cessou<sup>b</sup>, B. Lecordier<sup>b,\*</sup>

<sup>a</sup>*Department of Aerospace Engineering, Indian Institute of Science, Bangalore, 560012, India.*

<sup>b</sup>*Normandie Univ., UNIROUEN, INSA Rouen, CNRS, CORIA, 76000 Rouen, France*

---

## Abstract

The present work investigates the effect of jet-exit Reynolds number ( $Re$ ) on soot particle size and flame temperature in  $n$ -butane jet flames. Correlation of temperature with soot volume fraction ( $f_v$ ), soot precursor (polycyclic aromatic hydrocarbons or PAH), and reaction zone (OH) is also examined. The investigated flames ( $Re = 5000$  to  $21500$ ) are identical as of the companion work (Part 1). The temperature was measured in a low-sooting region using a fine-wire thermocouple. The soot particle size distribution was obtained using a scanning mobility particle sizer (SMPS). Temporal evolution (with  $0.1$  s resolution) of  $f_v$  in the extracted aerosol sample was monitored with a Pegasor particle sensor (PPS).  $f_v$  from LII and PPS are compared, and the reasons for differences are discussed in detail. The radial location of peak temperature is biased towards the fuel-rich side. At  $Re$  5000, peak-PAH occurs at  $650$  K, whereas in lifted turbulent flame ( $Re$  21500), peak-PAH shifts to  $940$  K. PAH formation temperature is influenced by air/fuel mixing. Despite the variation of turbulence level ( $Re = 5000 - 21500$ ), peak- $f_v$  in the soot inception region occurs at a nearly identical temperature of  $1400$  K. Peak- $f_v$  shifts towards lower temperature with increasing height, likely due to oxidation by diffused OH. The soot mode diameter ( $D_m$ ) was measured along the axis.  $D_m$  increases with height and reaches a maximum near peak- $f_v$  region.  $D_m$  at moderate  $Re$

---

\*Corresponding author:

*Email address:* `bertrand.lecordier@coria.fr` (B. Lecordier)

(5000 – 21500), varies between 12 – 28 nm along the flame axis. At high  $Re$  (21500),  $D_m$  range decreases to 12 – 24 nm. The decrease in peak- $D_m$  with  $Re$  is likely due to reduced residence time and enhanced reactant mixing. The comprehensive database containing a wide range of parameters from the present and companion (Part 1) papers will aid in the development and validation of turbulence and soot chemistry models, especially for fuels of practical relevance.

*Keywords:* turbulent sooting flames, butane, soot, SMPS, soot particle size

---

## 1. Introduction

This is the second paper of a two-part series on the characterization of sooting  $n$ -butane jet flames. In turbulent flows, to predict soot formation, turbulence and soot chemistry processes are modeled. These models are generally assessed against an experimental database. Therefore, the database-oriented works have been reported in turbulent sooting flames, both in jet [1–3] and swirl stabilized [4–7] flame configurations. These databases proved to be valuable in the assessment of numerical models in turbulent jet [3, 8] and swirl [9–12] flames. These past studies primarily focused on ethylene fuel owing to high soot yield and well-established chemical kinetics. However, investigations of soot formation in larger alkanes such as  $n$ -butane are necessary to develop soot chemistry models for fuels of practical relevance. Thermochemical and combustion characteristics of  $n$ -butane are similar to the fuels of practical interest [13, 14].  $n$ -butane is the smallest paraffin that mimics oxidation of larger paraffins contained in gasoline [15]. Therefore, to validate soot models intended for practical fuels, there is a need for a benchmark database with surrogate fuels besides ethylene. For these reasons, we comprehensively characterized sooting  $n$ -butane jet flames using a range of experimental methods. The companion paper [16], focuses on the effect of jet-exit Reynolds number ( $Re$ ) on soot concentration, soot precursors, and reaction zone. Laser-induced fluorescence (LIF) and laser-induced incandescence techniques (LII) were used to obtain the data non-intrusively. The present paper (Part 2) investigates the effect of  $Re$  on soot size and soot-temperature

correlations in identical  $n$ -butane jet flames [16], including the turbulent flow condition.

25 In Part 1 [16], previous studies in turbulent sooting jet flames are reviewed in detail. Therefore in this part, the literature focused on temperature and soot size are discussed. For a given fuel, the soot formation process depends on the following local conditions, namely mixing field, velocity field, residence time, and temperature. In turbulent flame, many of these local properties fluctuate  
30 simultaneously, which poses difficulty in assessing the impact of an individual parameter on soot formation. The temperature is one of the most important quantities which governs soot formation and oxidation. The investigation by Coppalle and Joyeux [17] provided correlations between temperature and soot volume fraction ( $f_v$ ) in ethylene jet flames at different  $Re$ . The authors [17]  
35 used an optical probe, which provided extinction-based  $f_v$ , while the temperature was deduced through two-color pyrometry. Such optical probe-based  $f_v$  and temperature were also reported by Shaddix et al. [18]. Although the technique provides simultaneous measurements, the probe perturbation and low spatial resolution are the limitations. Chan et al. [19] reported temperature and soot  
40 concentration in laminar flames using two-line LIF thermometry and LII. The flame wrinkling was demonstrated [19] to have an impact on soot-temperature correlations. A similar measurement technique was applied to turbulent flames [20], where a strong correlation between soot presence and a certain temperature range was noted. Kohler et al. [2] measured temperature in turbulent ethylene  
45 jet flame using coherent anti-stokes Raman scattering. Gu et al. [21] investigated a similar flame by simultaneously measuring temperature,  $f_v$ , and soot size. Joint statistics between various parameters, including  $f_v$  and temperature, were reported. A similar measurement approach was employed by Kruse et al. [22] to investigate soot oxidation in turbulent toluene flame. Park et al. [23]  
50 compared the temperature deduced from Krypton LIF with the fine-wire thermocouple measurements. An excellent agreement between the thermocouple and LIF-based measurements was demonstrated. Park et al. [24] used Krypton LIF to investigate  $f_v$  and temperature correlations in the soot inception region of

nitrogen-diluted ethylene flame. These investigations [19–24] suggest a preferred  
55 temperature range (typically, 1200 – 1600 K) where  $f_v$  peaks. Besides ethylene  
flame, it is of interest to assess such soot-temperature correlations in  $n$ -butane  
flames since its oxidation chemistry is similar to that of larger paraffins present  
in practical fuels. In the present work, the temperature was measured in low-  
sooting regions using a fine-wire thermocouple. The mean temperature profiles  
60 are compared with the time-averaged  $f_v$  from LII to investigate correlations.

Soot particle size can also be used to validate simulation models, as in Ref.  
[12]. The soot particle diameter can be measured either in a traditional *ex-situ*  
manner or using non-intrusive optical techniques. Time-resolved LII (TR-LII)  
can provide the primary diameter ( $d_p$ ) of soot aggregates but not the aggregate  
65 size. To obtain the soot aggregate size, TR-LII and elastic scattering techniques  
were combined [25] to obtain the radius of gyration ( $R_{gy}$ ) and the number of  
primary particles per aggregate ( $N_p$ ). Such complete description ( $f_v$ ,  $d_p$ ,  $R_{gy}$   
and  $N_p$ ) of soot concentration, soot size, and morphology has been reported in  
laminar ethylene flame [25]. In turbulent ethylene flame, Gu et al. [26] reported  
70 the axial variation of soot primary diameter ( $d_p$ ), based on TR-LII. The  $d_p$   
measurements were also reported in toluene flame [22].

A scanning mobility particle sizer (SMPS) is an *ex-situ* technique which can  
provide the soot particle size distribution (PSD) and concentration. Note that  
SMPS measures the size of a soot aggregate (mobility diameter,  $d_m$ ). Thus,  
75 the SMPS-derived aggregate size ( $d_m$ ) will differ from LII-deduced  $d_p$ . In low-  
sooting  $n$ -butane laminar flames [27], a good agreement between LII- and SMPS-  
based soot sizes is demonstrated. Agreement between mode  $d_m$  and  $d_p$  in [27]  
suggests no soot aggregation in a nascent soot particle. Several studies have  
reported soot PSD in laminar ethylene flame using SMPS. Zhao et al. [28]  
80 observed a unimodal PSD in the inception region, which subsequently developed  
a bimodality with increasing height above the burner. The bimodality was solely  
associated with primary particles [29]. The work of Gu et al. [26] showed that  
the PSD shapes are highly sensitive to the flame temperature and equivalence  
ratio. Such PSD studies in  $n$ -butane flames are relatively few [30], even in

85 laminar flows.

In turbulent flames, very few studies report the SMPS-based soot particle size. Soot PSD has been measured in swirl-stabilized ethylene flames by De Falco et al. [7]. Chowdhury et al. [31] and Boyette et al. [32] measured the soot particle size in turbulent nitrogen-diluted ethylene jet flames. The nitrogen  
90 dilution was necessary to avoid the blockage of the sampling orifice due to soot deposition. In undiluted flames (present case), a larger soot yield can result in uncertainty if the sampling orifice gets clogged. Therefore, it is necessary to monitor the temporal evolution of soot concentration in the extracted sample. Thus, along with SMPS, we also employ a Pegasor particle sensor (PPS) to  
95 monitor the soot concentration temporally with 0.1 s resolution. Soot concentration from PPS is used to incorporate the orifice blockage correction of the SMPS data. PPS has generally been used to measure particulate emissions from internal combustion engines [33–35]. In fundamental combustion research, PPS has not yet been used widely.

100 The primary intention of the present work is to report a part of the comprehensive database needed for the validation of soot models relevant to turbulent *n*-butane flames. Further objectives are to *i*) Investigate correlations between temperature and various parameters reported in Part 1 [16], namely  $f_v$ , PAH, and OH, on the time-averaged basis, and *ii*) Assess the effect of jet-exit  $Re$  on  
105 soot particle size.

## 2. Experimental methods

### 2.1. Burner and Flame condition

The measurements were performed in *n*-butane non-premixed jet flames at atmospheric pressure. The burner geometry and flame conditions are detailed  
110 in Part 1 [16]. *n*-butane was issued through a 2.4 mm tube in the co-flowing air. The flames were enclosed in a square duct (400 mm wide and 750 mm high) through which co-flow air was issued. The air co-flow was maintained at 5 g/s, which is high enough to ensure the over-ventilated flame condition. The flow

rates were regulated by Coriolis-calibrated thermal mass flow controllers [16].  
115 The uncertainty in flow rates is estimated to be within  $\pm 1\%$ . Three *n*-butane  
flames (*Re* 5000, 7200, and 21500) out of the four cases investigated in [16] are  
considered. The *Re* 2100 flame was not suitable for intrusive measurements  
due to large soot concentration and low jet momentum, which could result in  
significant probe-induced perturbations.

120 *Re* is defined based on the jet-exit bulk velocity and tube diameter. Gener-  
ally, the turbulence level increases with *Re* [36]. Therefore, *Re* has been used  
[37, 38] as a global parameter to represent the overall turbulence level. *Re* was  
varied from 2100 to 21500 by changing the fuel flow rate from 0.03 to 0.3 *g/s*.  
Consequently, *Re* variation was accompanied by a change in residence time since  
125 the bulk velocity (flow rate) was altered. Therefore, to assess the effect of local  
turbulence, the velocity field needs to be measured (e.g., [39]). In the present  
work, the local velocity was measured only for *Re* 21500 in the jet-exit region.  
Thus, the effect of local turbulence on soot could not be assessed explicitly.

*Re* 5000 flame was attached to the fuel tube, while *Re* 7200 and 21500  
130 flames were lifted with 11 and 53 mm lift-off heights, respectively [16]. From  
the modeling point of view, a database of the attached flame is preferred [1]  
due to difficulty in modeling lifted flames owing to the partial premixing at the  
flame base. In general, a pilot flame has been used [1] to avoid the lift-off at high  
*Re*; however, the pilot flame is argued [2] to introduce modeling complexities.  
135 Another approach is to use an additive in fuel or oxidizer stream, such as H<sub>2</sub>  
[40] or O<sub>2</sub> [41] to keep the flame attached. This approach was not used in the  
present work since the database with pure *n*-butane was intended. Instead, we  
provide the precise velocity and mixing fields in a lifted part of the flame (for  
*Re* 21500) as boundary conditions.

## 140 2.2. Laser diagnostics

The present paper uses the soot concentration, soot-precursor (PAH), and  
flame location (OH) data obtained in the companion work [16]. A brief descrip-  
tion of the measurement methods is provided here, while detailed information

can be found in [16]. Soot volume fraction was measured using the LII technique. Soot particles were heated by a 1064 nm wavelength pulse (from a Nd:YAG laser), and the resulting incandescence signal was acquired at 400 nm. The average laser fluence of 0.4 J/cm<sup>2</sup> was used to ensure the plateau regime of LII. The LII signal was imaged on an intensified CCD (ICCD) camera with a prompt gating of 50 ns relative to the laser pulse. To obtain the soot volume fraction, the LII signal was calibrated using a laser-extinction measurement at 1064 nm. To image OH and PAH distributions, the planar laser-induced fluorescence (PLIF) technique was used. The OH radical was excited using 283 nm wavelength (from a dye laser) with 0.05 J/cm<sup>2</sup> average fluence. The resulting OH fluorescence was imaged at 310 nm using an emICCD camera gated to 30 ns width. PAH is excited with 283 nm wavelength laser pulse at a reduced fluence (0.02 J/cm<sup>2</sup>) to avoid the LII interference. The PAH-PLIF signal was acquired in a 350 – 400 nm range with an ICCD camera gated to 50 ns width. These excitation and detection parameters provide the LIF signal primarily from 2-4 ring PAH [42]. In all the above diagnostics, the signal was imaged at a magnification of 5.75 pixels/mm, which corresponds to 89 mm wide field-of-view (FOV). A total of 1000 to 2000 images (depending on height above the burner) were acquired at a 10 Hz rate. The time-averaged data sets of  $f_v$ , OH-PLIF, and PAH-PLIF from [16] are used in the present paper to investigate their correlations with temperature.

### 2.3. Temperature measurements

The gas temperature was measured using a fine-wire thermocouple. A Type-B thermocouple (Pt-30%Rh / Pt-6%Rh) was chosen due to its high temperature limit. Thermocouple wires of 50 μm diameter were butt-welded to form a junction. The junction was exposed to the flame, while the extension wires were shielded in a twin-bore ceramic tube. The thermocouple signal was amplified and digitized at a 3 kHz rate. The lowest measurable temperature was limited to 530 K due to a weaker thermocouple signal. The thermocouple was traversed through the flame using a 3-axis motorized stage. The translation

stage and data acquisition system were integrated to automate the measure-  
175 ments. Any misalignment between the thermocouple translation and flame axes  
was minimized through a 2D temperature mapping at two different heights  
(planes). This provided the flame axis and its orientation with reference to the  
thermocouple translation coordinates.

Temperature measurements are intended to be quantitative. Therefore, vari-  
180 ous uncertainty sources, namely 1) calibration error, 2) catalytic effects, 3) local  
flame perturbations, and 4) radiation correction uncertainty, are assessed. The  
calibration accuracy was verified by measuring known temperatures (within the  
570 – 1060  $K$  range) in a portable calibration furnace (Pegasus 1200B, AOIP).  
The conduction heat losses through thermocouple wires can be neglected since  
185 the wire length was long (10  $mm$ ) relative to the diameter (50  $\mu m$ ). In reduc-  
ing atmospheres, the platinum surface can act as a catalyst that may enhance  
exothermic reactions. A non-catalytic coating could have been used; however,  
such coating deteriorates the temporal response in turbulent flames. Therefore,  
the uncoated bare thermocouple was used. The catalytic effects in non-premixed  
190 flames were speculated to be insignificant due to lower radical concentration [43].  
This is confirmed by an excellent agreement between LIF-based temperature and  
thermocouple (uncoated) measurements that are reported by Park et al. [23].  
Nevertheless, we assessed the catalytic effects by traversing the thermocouple  
from oxidizer to fuel stream and vice-a-versa. The hysteretic effects were not  
195 significant in the present flames (see Fig. S1 in Supplement).

Since the thermocouple size was small (50  $\mu m$ ), no significant flame pertur-  
bations were noted, as evidenced from Fig. 1, where lift-off height and overall  
flame appearance with and without the thermocouple are identical. The mea-  
surements stations are marked on respective flame photographs in Fig. 2. The  
200  $Re$  5000 flame is attached, while other flames are lifted. The lift-off heights for  
 $Re$  7200 and 21500 measured 53 and 11  $mm$ , respectively, based on OH-PLIF  
data [16]. Since the  $Re$  2100 flame was highly sooting, the temperature was  
not measured. In remaining flames, measurements were limited to low-sooting  
regions, where time-averaged  $f_v$  is below 0.1  $ppm$  (deduced from LII measure-

205 ments in [16]). The soot deposition can change the emissivity and diameter of  
the thermocouple junction, consequently resulting in a large uncertainty. To  
reduce the effect of soot deposition, the measurement duration was limited to  
3 s at each location. In the case of soot deposition, the temperature was re-  
ported to decrease even within the first two seconds [43]. Over the present 3 s  
210 duration, the temperature did not decay (see Fig. S2), which suggests negligible  
soot deposition. Additionally, no visible deposition was noted at the end of mea-  
surements. The radiation correction is necessary since the flame temperature is  
anticipated to be high ( $T_{ad} = 2267\text{ K}$ ). The correction is applied by considering  
a convection-radiation balance as detailed in Sec. S1.3 of the Supplement.

215 The detailed estimates of uncertainties owing to errors in radiation cor-  
rection, positional error, and statistical uncertainty in mean temperature are  
provided in Sec. S1.4. The combined uncertainty in mean temperature at a  
peak value (2250 K) is estimated to be  $\pm 6\%$ , while uncertainty is  $\pm 4\%$  in the  
temperature range of 600 – 1600 K.

#### 220 2.4. Particle analyzers

A Pegasor particle sensor (PPS) was used to measure the soot concentration,  
whereas the scanning mobility particle sizer (SMPS) was employed to measure  
the soot particle size simultaneously. Both SMPS and PPS measurements re-  
quire the extraction of an aerosol sample from the flame. Figure 3 shows the  
225 schematic of the experimental layout. The sample was drawn through a 1 mm  
orifice drilled in a probe tube of 4 mm inner diameter and 1 mm wall thickness.  
To draw the sample, a mild vacuum was generated by a pump. The suction  
strength was controlled by a valve. The sample was quickly diluted with nitro-  
gen ( $N_2$ ) that was issued through the tube at a 10 liters per minute (*lpm*) flow  
230 rate. The  $N_2$  dilution assists in quenching of reactions, and it also limits the  
soot aggregation. Apart from  $N_2$ , additional dilution (with air) was achieved  
using two diluter units (VKL 10, PALAS) connected in tandem. This provided  
an additional dilution factor of 100. Such a heavy dilution is necessary to avoid  
the saturation of SMPS and PPS.

235 The probing system and dilution level were qualified using a well-characterized  
miniCAST soot (miniCAST 5200, Jing) generator. Soot generated by mini-  
CAST propane (0.06 *lpm*)/air (1.5 *lpm*) flame was very stable and reproducible.  
The combustion products (including soot) were quenched by nitrogen gas (7 *lpm*).  
The products were further diluted with air (20 *lpm*) within the miniCAST sys-  
240 tem. Next, the SMPS measurements were performed at various  $N_2$  flow rates  
through the probe. Subsequently, 10 *lpm* was found to be enough to avoid  
soot aggregation in the sampling line, as inferred from the converged soot PSD,  
similar to [32, 44]. For the miniCAST configuration, PPS measurement showed  
remarkable stability in the soot concentration with time, indicating no block-  
245 age of the orifice. The dilution ratio ( $N_2$ /sample) is determined to be 24:1 by  
comparing PPS measurements with the probe and directly without the probe.  
Recall, the additional air dilution ( $\times 100$ ) was used. Thus, the effective dilution  
ratio was 2400:1 by volume. The sample extraction set-up was identical (valve  
position, vacuum pump, etc.) as of the main campaign. Therefore, the dilution  
250 ratio deduced in miniCAST was used to calibrate the measurements performed  
in butane jet flames. Uncertainty in the dilution ratio is discussed subsequently  
in Sec. 3.3.

The sampling probe generally perturbs the flame through alteration of lo-  
cal temperature and upstream flow-field. Yet, a wealth of information can be  
255 extracted with fewer assumptions and lesser complexity than laser-based tech-  
niques. In laminar flames, perturbations are contained within a few *mm* up-  
stream of the probe [29]. In the turbulent flame, upstream perturbations are  
expected to be lower due to larger flow momentum. Figure S4 in the Supplement  
shows flame photographs with the probe, suggesting low global perturbations.  
260 Although, a discrepancy exists between LII and probe-derived soot concentra-  
tion, especially at low  $Re$  (discussed in Sec. 3.3).

PPS (PPS-M 2000HC PEMS, Pegasor) provides the quasi-temporally re-  
solved (0.1 *s*) soot concentration. In the PPS technique, soot particles interact  
with ionized air. The exiting charged particles provide an estimate of escaping  
265 current, which is proportional to the soot concentration. A detailed working

principle can be found in Ref. [35]. Once the escaping current ( $I_{pps}$ ) is measured, soot mass concentration can be deduced as  $C_s = K_{pps} \cdot I_{pps} / Q_v$ , where  $Q_v$  is the sample flow rate (5 *lpm*) and  $K_{pps}$  is a constant (1.05, based on Diesel soot applications [45]). Next, the soot volume fraction can be deduced as  $f_v\text{-PPS} = C_s / \rho_{soot}$ , where  $\rho_{soot}$  is a soot particle density which is assumed to be 1700  $kg/m^3$ , based on a range of values reported in the literature (1500 [29] - 1900 [46]  $kg/m^3$ ). The combined uncertainty in PPS is estimated to be  $\pm 56\%$ . Individual error sources are discussed subsequently in Sec. 3.3.

The SMPS system (Classifier 3080 + CPC 3010, TSI) was used to obtain the soot particle size distribution. The aerosol sample was supplied to the instrument at 1 *lpm* flow rate, while the sheath flow rate was set to 10 *lpm*. SMPS counts the particle concentration by a sequential selection of classes of electrical mobility diameters over a specific range. Such scan duration is long (2 *min* for 7 – 290 *nm*), and thus, SMPS is generally used in laminar flames [26, 28–30]. Nevertheless, for the size range of interest (mode diameter 7 – 30 *nm*), the scan duration was short (23 *s*). The relative uncertainty in the particle size distribution shape is estimated to be 10% based on Ref. [32].

### 3. Results and discussion

#### 3.1. Flame temperature

Temperature measurements were performed in low-sooting regions, where time-averaged  $f_v$  was less than 0.1 *ppm*. Figure 4 shows the radiation corrected temperature profiles. In the case of turbulent flame (Fig. 4e), measurements for  $y < 60$  *mm* were not performed since the flame was lifted. Recall, the present thermocouple could not measure temperature below 530 *K*. To eliminate biased results, a dataset containing even a single instant of  $T \leq 530$  *K* was not retained. Therefore, the mean temperature is not available in some cases.

The peak flame temperature in *Re* 5000 flame at  $y = 10$  *mm* in Fig. 4a measures 2261 *K*, while  $T_{ad}$  is 2267 *K*. At  $y = 10$  *mm*, the soot concentration is negligible. Nevertheless, the temperature in non-premixed flames is expected

295 to be lower than  $T_{ad}$ . Recall, at high temperature,  $\pm 6\%$  uncertainty (detailed in  
 S1.4) exists. The actual peak flame temperature is likely to be lower. In  $Re$  7200  
 flame, peak temperature (in Fig. 4c) at  $y = 10$  mm is lower due to a lifted flame  
 base (see Fig. 2b). The lift-off height for this flame measures 11 mm with  
 a standard deviation ( $\sigma$ ) of 0.6 mm based on the OH-PLIF data [16]. At  $y =$   
 300 10 mm, the flame leading edge spatially fluctuates. Therefore, the thermocouple  
 is subjected to fluctuations between preheat and post-flame zones, which lowers  
 the mean temperature. For a given  $Re$ , in general, the temperature decreases  
 with increasing  $y$ . In  $Re$  5000 flame (Fig. 4a), the radial peak temperature  
 reduces by  $\sim 150$  K with increase in height from  $y = 10$  to 60 mm. The soot  
 305 radiation effect [47] alone cannot explain the observed drop in temperature since  
 the measurements were restricted to low  $f_v$  regions. Recall that the plotted  
 temperatures in Fig. 4 are time-averaged. In addition to mean, we also deduce  
 root mean square (RMS) values. This data is provided in the Supplementary  
 material. Since the thermocouple response time is estimated to be 10 ms, RMS  
 310 values are indicative. Nonetheless, RMS can be compared on a relative basis  
 across flames and measurement locations. The unsteadiness of the jet flames  
 increases with height, as noted from increasing RMS values of temperature.  
 Consequently, the thermocouple is subjected to spatial fluctuations between  
 the peak (reaction zone) and moderate (preheat zone) temperature regions of  
 315 the flame. Thus, the time-averaged temperature decreases with height.

With increasing  $Re$ , the peak flame temperature drops, accompanied by the  
 increased profile widths. The flame stretch increases with  $Re$  due to increased  
 flame wrinkling (curvature) and flow strain, consequently lowering the instanta-  
 neous flame temperature. The mean temperature further reduces due to spatial  
 320 fluctuations of the flame and associated time-averaging, as discussed earlier.  
 Temperature profiles become broader due to increased flame-brush thickness  
 with  $Re$ . In Fig. 4, the thermocouple enters from left ( $r^-$ ) to right ( $r^+$ ).  
 Temperature profiles are minutely asymmetric, which is attributed to the ther-  
 mocouple perturbation towards  $r^+$  side in Fig. 4. Even this mild asymmetry  
 325 could influence the temperature correlations with OH, PAH, and soot. Thus,

only the left side ( $r^-$ ) of the profile is retained for further analysis.

### 3.2. Temperature correlations

Temperature profiles are used to deduce correlations with soot concentration, soot-precursor (PAH), and reaction zone (OH) reported in the companion paper  
330 [16]. To visualize the spatial trends, the profiles are extracted from the time-averaged planar data. Figure 5 shows PAH-LIF,  $f_v$ , and OH-LIF profiles at  $y = 100 \text{ mm}$ , for  $Re$  2100, 5000, and 7200 flames. Recall, temperature measurements in  $Re$  2100 are not available. However, OH, PAH, and  $f_v$  are available, and thus presented to enable comparison with other  $Re$ . For turbulent flame, the profiles  
335 at  $y = 250 \text{ mm}$  (where  $f_v$  is appreciable) are plotted. A peak asymmetry is noted in  $f_v$ , which is attributed to possible beam steering and laser extinction along the path [37]. Therefore following Sun et al. [37] data only towards the laser-incident side is retained.

At  $Re$  2100 (Fig. 5a), the radial order of the species from the jet axis is as  
340 following: PAH, soot, and reaction zone. A minute OH-LIF signal near the jet core is attributed to interference from 1-2 ring PAH, as discussed in [16]. The radial order of species is the result of temperature and air/fuel mixing field. At a low oxygen concentration and a certain temperature range (700–1300 K [48]), PAH forms through pyrolysis of fuel. The smaller PAH gets converted to larger  
345 PAH with increasing temperature. Subsequently, larger PAH coagulate and go through thermochemical processes to eventually form a nascent soot particle [49]. Next, soot particles grow through aggregation and surface reactions. Soot eventually gets oxidized in the vicinity of the flame, primarily through the OH route [50]. With an increase in  $Re$ , the PAH peak shifts from flame wing to the  
350 jet axis, while the annular structure of soot and reaction zone is preserved. The mass diffusion of the solid soot particles is negligible relative to the diffusion of gaseous species (PAH) [51]. In the turbulent flame (Fig. 5d), the time-averaged profiles become much broader than that of the laminar flame. The broadening of profiles is related to the spatial fluctuations induced by turbulent structures.

355 *3.2.1. Temperature correlation with OH*

The radial peak locations of OH-LIF and temperature are compared for different flames in Fig. 6 at several heights. The temperature profiles are much broader than that of the OH, even in the laminar flame (Fig. 6a). The OH peak and temperature peak lie close to each other; however, the temperature-peaks (and -profiles) are biased towards the fuel stream. In a non-premixed flame, combustion generally occurs at a stoichiometric surface, with products distributed on either side of the reaction zone. OH peaks in close vicinity of the stoichiometric surface but towards the fuel-lean side, as demonstrated by Donabar et al. [52] in a turbulent jet flame. Consequently, OH and temperature peaks do not overlap. In premixed flames, temperature peaks at a fuel-rich condition ( $\phi = 1.05$  for *n*-butane). The appreciable shift of the temperature peak relative to OH in Fig. 6 suggests the occurrence of peak-temperature at even richer  $\phi$ . The observation deduced from Park et al. [24] indicates the occurrence of peak-temperature at  $\phi \sim 1.2$  in a turbulent jet flame. In non-premixed flames, apart from chemical kinetics, convection and diffusion processes determine the peak-temperature  $\phi$  [53]. In the present flame, to identify  $\phi$  corresponding to the peak-temperature, the mixture fraction data is needed.

370 *3.2.2. Temperature correlation with PAH*

The PAH-LIF profiles are also compared with the temperature in Fig. 7 for different *Re*. In turbulent flame (*Re* 21500), no appreciable PAH is detected at lower height since the flame is lifted. In general, PAH concentration peaks in the fuel-rich low temperature zone. For quantitative comparison, temperature value at peak-PAH location is provided in Table 1. In the attached flame (*Re* 5000) at the base, PAH peaks at a much lower temperature (650 K). Since reactant premixing is nearly absent in the attached flame, pyrolysis of fuel (that assist in PAH formation) may take place at a lower temperature. PAH peak shifts towards higher temperature with increasing height. This trend is likely associated with the increased diffusion of air with residence time (which is proportional to height). The presence of oxygen can shift the PAH formation to a

385 higher temperature.

Conversely, in a lifted flame ( $Re$  7200), the PAH peak appears to be less sensitive to height. The oxygen content in the PAH formation zones may not be varying significantly in the  $y = 20 - 120$  mm region due to partial premixing. At  $y = 20$  mm, the PAH peak occurs at a much higher temperature than that in  
390 the attached flame. A partial premixing in the lifted region is likely responsible for the observed trend. In the turbulent flame ( $Re$  21500), higher lift-off height ( $h_{lift} = 53$  mm) and turbulence cause stronger premixing at the flame base. Therefore, the peak-PAH occurs at an even higher temperature of 940 K. With increasing  $Re$ , the residence time decreases while mixing enhances. The results  
395 show that the PAH formation temperature is influenced by the air/fuel mixing and residence time.

### 3.2.3. Temperature correlation with soot concentration

The temperature-soot correlations are explored in a similar manner. For such correlations, generally, simultaneous measurements of temperature and  
400 soot have been performed. However, there is likely to be a notable (few ms) delay between a change in local flow conditions and soot response, as evidenced from time-resolved measurements of Stöhr et al. [54]. Owing to longer soot reaction timescales (few ms), interpretation of instantaneous correlation is difficult in turbulent flames. The influence of soot response delay on time-averaged corre-  
405 lation is expected to be less significant than that of instantaneous correlation for a statistically stationary flow. To understand time-resolved soot-temperature correlation, high-speed simultaneous diagnostics is required where quantification is not trivial. Therefore, in this work, only time-averaged correlations are assessed.

410 Figure 8 shows the mean temperature and  $f_v$  profiles in  $Re$  7200 flame. Soot lies closer to the fuel-rich zone, away from the peak temperature location. The spatial trend between soot and temperature is similar to that reported in turbulent diluted ethylene flame by Park et al. [23]. The width of the temperature profile is larger than the  $f_v$  profile. This observation is similar

415 to that of Gu et al. [21]. In general, soot structures are highly localized due  
to a large Schmidt number of soot particles, which leads to a low soot mass  
diffusivity [55] relative to the thermal diffusivity of a gas. Consequently, the  
temperature profile width outgrows the soot profile width, as observed in Fig.  
8. Similar to  $Re$  7200 flame, the temperature and  $f_v$  profiles are overlaid for  
420 other flames (but not shown for brevity).

Soot exists within a certain temperature range. To enable quantitative compar-  
ison, we deduce the mean gas temperature where time-averaged  $f_v$  peaks.  
Figure 9 shows temperature profiles at select heights, along with the radial loca-  
tion of peak  $f_v$  and corresponding temperature ( $T_{f_v^{pk}}$ ). In  $Re$  5000 flame,  $T_{f_v^{pk}}$   
425 drops from 1400 to 1200 K with height in a  $y$  range of 30 to 120 mm. Note,  
the  $T_{f_v^{pk}}$  trend is opposite of the temperature-PAH correlation where the tem-  
perature corresponding to peak-PAH increased with height. In  $Re$  7200 flame,  
 $T_{f_v^{pk}}$  decreases similarly from 1400 to 1300 K when  $y$  increases from 60 to 120  
mm. The  $y$  range for  $Re$  7200 is different than the  $Re$  5000 case to account  
430 for varying soot inception heights. The plot for  $Re$  21500 flame is not shown  
since measurable  $f_v$  and  $T$  are available only at  $y = 120$  mm. In this turbulent  
flame, peak  $f_v$  occurs around 1400 K (at  $y = 120$  mm). Despite the variation  
of turbulence level ( $Re$ ),  $T_{f_v^{pk}}$  at soot inception regions is almost identical with  
a value of 1400 K. This optimum temperature is the result of a competition  
435 between soot formation and oxidation reactions. Soot formation is dominated  
by larger PAH, while oxidation is primarily influenced by OH [26]. In the vicini-  
ty of flame, soot reaction with diffused OH can reduce the soot concentration.  
Consequently,  $f_v$  peaks away from the high-temperature regions of the reaction  
zone.

440 The possible reasons for the decrease in  $T_{f_v^{pk}}$  with height are discussed  
next. The peak flame temperature itself decreases with height due to the time-  
averaging of unsteady flame, as discussed earlier. Apart from this, the nascent  
soot during inception may require higher temperatures to form. Conversely, at  
downstream locations, the soot growth is facilitated by surface reactions and  
445 transported PAH from upstream regions. The residence time also increases

with height, which may decrease  $T_{f_v^{pk}}$ . With increasing height, OH may diffuse into the fuel-rich regions through diffusion and convective transports. As OH is the dominant soot oxidizer,  $f_v^{pk}$  could shift to a lower temperature region with height.

450 The present findings are compared with the measurements in ethylene flames, since such data in turbulent *n*-butane flame is not yet reported. Note that the stoichiometric  $T_{ad}$  of *n*-butane flame is  $\sim 100$  K lower than that of the ethylene. In turbulent ethylene lifted DLR jet flame ( $Re = 10000$ ), the peak  $f_v$  was reported [21] to exist in a 1550 – 1750 K range. This range is compar-  
 455 ble to the  $T_{f_v^{pk}} \approx 1600$  K reported by Coppalle and Joyeux [17] in ethylene flame at  $Re = 11800$ . In a different ethylene flame ( $Re = 20000$ , pilot stabilized)  $T_{f_v^{pk}} \approx 1400$  K was reported [18]. Higher  $Re$  could lead to lower flame temperature due to increased flame-stretch. Additionally, measurements in [18] were path integrated over a larger region (10 mm), resulting in lower resolution.  
 460 From a LIF-based temperature measurement in a diluted turbulent ( $Re = 8300$ ) ethylene flame [23, 24], peak  $f_v$  was shown to occur in a 1300 – 1500 K range in the soot inception region. This temperature range is lower compared to pure ethylene flames [17, 21], but lies closer to [18]. Park et al. [23] argued that with a diluted fuel, the flame temperature itself is lower, consequently resulting in  
 465 a low  $T_{f_v^{pk}}$ . In the present *n*-butane flames,  $T_{f_v^{pk}}$  at the soot inception region (1400 K) is in agreement with a diluted ethylene flame of Park et al. [23, 24].

### 3.3. Soot concentration from PPS

The PPS-based soot concentrations are compared with that of LII from the companion work [16]. Note, the use of PPS was primarily intended to monitor  
 470 the temporal evolution of the soot sample during an SMPS scan. Figure 10 shows the temporal evolution of soot volume fraction in aerosol sample extracted from  $Re$  7200 flame at  $y = 250$  mm. The profile shows the initial spike as flame ignites. Subsequently,  $f_v$  decreases due to the blockage of the probe orifice. The peak concentration associated with the flame transition is not retained. There  
 475 exists a distinct post-peak transition marked by a circle (in Fig. 10), which

is assumed to be the quasi-steady soot concentration before any obstruction of the orifice. This procedure is adapted for all the measurements. The blockage of the probe orifice is lesser in the turbulent case due to lower  $f_v$ . The SMPS measurements are affected by the probe blockage over the scan time. Therefore,  
 480 the SMPS data is corrected using PPS measurements, as detailed separately in Sec. S2.2 of the Supplement.

Soot concentrations obtained from PPS ( $f_{v-PPS}$ ) are compared with that of the LII ( $f_{v-LII}$ ). Figure 11 shows the axial (centerline) mean profiles of  $f_{v-LII}$  along with  $f_{v-PPS}$ . The objective of this comparison is to assess the impact  
 485 of probe perturbation on the flame. Overall, there is a qualitative agreement between  $f_{v-PPS}$  and  $f_{v-LII}$ . At  $Re$  5000,  $f_{v-PPS}$  appears to be shifted towards lower height relative to  $f_{v-LII}$ . However, this discrepancy reduces with increasing  $Re$ . As  $Re$  increases, higher jet momentum results in lower probe perturbations. Additionally, at higher  $Re$ , the flame width increases, which reduces  
 490 the PPS probe sensitivity to radial misalignment as well as to probe-induced radial fluctuations of  $f_v$ . These factors result in a better qualitative agreement between PPS and LII with increasing  $Re$ .

Although the qualitative trends are in agreement, absolute values of  $f_{v-PPS}$  are much higher than  $f_{v-LII}$ . The factor is 2.4 for  $Re$  5000 and 7200 flames,  
 495 whereas it measures 2.8 for  $Re$  21500 flame. A discrepancy between *in-situ* (LII based) and *ex-situ* (SMPS based)  $f_v$  values is reported recently [7]. The authors [7] argue that their LII measurements were biased towards larger soot particles (i.e., low LII sensitivity to smaller particles), and thus leading to lower LII-based  $f_v$  relative to SMPS measurements. Note,  $f_{v-LII}$  in Fig. 11 is  
 500 obtained from time-averaging, while  $f_{v-PPS}$  is quasi time-resolved (averaged over 0.1 s). Additionally, spatial resolutions of LII and PPS differ. The in-plane magnification of LII is  $\sim 0.2$  mm, while the out-of-plane resolution is expected to be  $\sim 0.2$  mm based on the laser-sheet thickness. The PPS resolution is five times coarser (1 mm) than LII. The larger probe volume and finer temporal  
 505 resolution of PPS eliminate the soot intermittency effect as the soot is always present in the sample. Additionally, due to *ex-situ* nature of PPS, soot sam-

ple may always be present in the sampling line. In contrast, significant soot intermittency is noted in spatially well-resolved LII measurements. Soot intermittency can lower  $f_{v-LII}$  when averaged unconditionally [16, 38, 56]. To  
510 isolate the effect of intermittency, the LII data can be conditionally averaged by considering samples only with the soot presence. The conditionally averaged peak axial  $f_{v-LII}$  measures nearly 3 times (2.8, 3.1, and 3.5 for  $Re$  5000,  $Re$  7200, and  $Re$  21500 respectively) as of the time-averaged one [16]. This factor is quite close to the ratio of time-averaged LII to PPS measurements  
515 shown in Fig. 11. The peak axial values of soot concentration from PPS and that of the conditionally averaged LII data are indeed in a reasonable ( $\pm 15\%$ ) agreement.

Various sources of uncertainty in soot measurement are discussed next. Although assumed to be robust, uncertainty in LII can arise from the following  
520 sources. 1) Uncertainty in extinction-based LII calibration due to beam steering was verified to be insignificant. The mean  $f_v$  value in a lifted ethylene flame ( $Re = 8700$ ) with the present LII set-up was available to enable validation with a similar flame ( $Re = 10000$ ) reported in [2, 21]. The mean peak  $f_v$  (0.56 ppm) was in close agreement with the value (0.54 ppm) reported in [2, 21]. 2) Un-  
525 certainty exists in the extinction coefficients  $K_e$  used for LII calibration.  $K_e$  varies with fuel and soot maturity (C-H composition) [57]. 3) The excitation laser beam steering in a turbulent flame can also affect the LII signal [37]. 4) Statistical uncertainty in the mean quantity arises due to fluctuations and a finite number of samples. The combined uncertainty (excluding  $K_e$ ) from the  
530 above sources is estimated to be  $\pm 19\%$  [16].

The uncertainty in PPS can arise from the following sources. 1) There is inherent uncertainty in PPS-derived  $f_v$  due to the transient nature originated from the probe blockage (recall Fig. 10). This uncertainty is estimated to be  $\pm 15\%$ , based on the signal fluctuations. 2) The conversion of the PPS signal  
535 to the soot mass concentration involves soot particle size distribution assumption, which can lead to uncertainty up to  $\pm 30\%$  [58]. Furthermore, soot mass concentration is converted to  $f_v$  through an assumed density, as indicated in

Sec. 2.4. The soot density typically varies from 1500 [29] to 1900 [46]  $kg/m^3$  with soot maturity. Therefore, we use 1700  $kg/m^3$  soot density accompanied by  $\pm 15\%$  uncertainty. 3) The uncertainty due to an error in probe positioning and upstream perturbations are estimated to be within  $\pm 5$  mm, which translates to  $f_v$  uncertainty of  $\pm 15\%$  based on LII fields [16]. 4) The absolute dilution ratio between the aerosol sample and  $N_2$  is estimated in a separate calibration burner (recall Sec. 2.4) at a different flow velocity and temperature than the jet flames. The flow velocity can affect the pressure upstream of the probe, while temperature influences the quench gas ( $N_2$ ) expansion. Therefore, the dilution ratio could differ, which may be the major source of uncertainty. The dilution uncertainty could be high as  $\pm 40\%$  [29].

Total uncertainty from the above sources is estimated to be  $\pm 56\%$  through propagation. Further investigation and quantification are difficult to pursue with the available data owing to the turbulent flow. The PPS data is primarily used to correct the SMPS results for probe blockage. This correction can be accomplished even with a relative soot concentration since only the particle size distribution is intended from SMPS than the absolute concentration. The PPS technique has not yet been widely used in the fundamental soot research community. The agreement (within  $\pm 15\%$ ) between  $f_{v-PPS}$  and conditionally averaged  $f_{v-LII}$  appears very promising, despite various uncertainty sources. This provides a base for technique-focused future works that could exploit PPS capabilities by addressing the aforementioned uncertainties. Unlike PPS, LII has been used widely (over a few decades) with a detailed understanding. Therefore, we retain only  $f_{v-LII}$  for the forthcoming analysis.

### 3.4. Soot particle size

#### 3.4.1. Soot particle size distribution

The soot particle size distributions (PSDs) at different heights ( $y$ ) are shown in Fig. 12 for  $Re$  5000 flame. Both raw and blockage-corrected PSDs are shown. The geometric mean diameter ( $D_g$ ) and standard deviation ( $\sigma_g$ ) are evaluated for both the corrected (C) and uncorrected (U) PSDs. Data within the entire

range (7–290 nm) of SMPS scan duration (120 s) is considered to evaluate  $D_g$  and  $\sigma_g$ .

570 In high-sooting regions ( $y = 310$  mm), large difference exists between  $\sigma_{gC}$  and  $\sigma_{gU}$  accompanied by much lower  $D_{gC}$ . This could be attributed to larger probe blockage with time. The data with orifice blockage  $> 95\%$  at the end of SMPS scan duration (120 s) is marked by \*. A high blockage can lead to uncertainties in correction, especially for larger soot size ( $> 60$  nm). Therefore, 575 the corrected data at  $y = 310$  and  $370$  mm should be interpreted with caution. As an alternative to  $D_g$ , a mode diameter (corresponding to the peak of PSD) can be evaluated. Note that the uncertainty in mode diameter ( $D_m$ ) due to blockage correction is not significant due to shorter SMPS scan duration over the range of interest (23 s until 30 nm, and 75 s until 60 nm).  $D_m$  could be 580 evaluated within  $\pm 5\%$  uncertainty from a given PSD.

Soot PSDs for  $Re$  7200 flame are shown in Fig. 13. The orifice blockage correction in unsteady (intermittent) flame-tip region ( $y = 525$  and  $580$  mm) and low-sooting region ( $y = 75$  mm) leads to increased fluctuations in PSD. On the other hand, the correction in a severe blockage case leads to high  $\sigma_{gC}$  with 585 lower  $D_{gC}$  at  $y = 250$ ,  $310$ , and  $370$  mm.

Similarly, PSDs for  $Re$  21500 flame are shown in Fig. 14. At lower measurement stations ( $y = 75$  and  $150$  mm), soot concentration (along the axis) is not appreciable. Thus, the lowest  $y$  station is different than  $Re$  5000 and 7200 flames. In turbulent flame, the probe orifice is the least blocked owing 590 to a low time-averaged soot concentration. Consequently,  $\sigma_{gC}$  and  $\sigma_{gU}$  are in close agreement. As the blockage is moderate, both  $D_{gC}$  and  $\sigma_{gC}$  are reliable throughout the measured axial locations.

All the PSDs (Figs. 12 to 14) exhibit a single mode within the present measurement range. This unimodality is in agreement with the PSD reported 595 in diluted ethylene jet flames [31]. However, LES investigation [8] in turbulent ethylene flame showed a bimodal PSD which is primarily prevalent downstream of the peak- $f_v$  location. The first mode [8] occurs at a much smaller diameter ( $< 5$  nm), while the detection limit of the present system is 7 nm. In turbulent

toluene flame, Kruse et al. [22] also noted a bimodal distribution of  $d_p$  in a soot  
600 oxidation region.

For a given  $Re$ , with increasing height ( $y$ ), soot particles are observed to be distributed over a wider size range, consistent with [21]. In inception regions (lower  $y$ ), generally nascent soot particles exist without any aggregation. At a higher height, surface growth of primary soot particles takes place in addition  
605 to aggregation. This leads to a wider particle size distribution in downstream regions. Excluding the high-sooting and flame-tip regions,  $\sigma_g$  in  $Re$  5000 flame (Fig. 12) appears to increase from 1.5 to 1.6  $nm$  with height. For  $Re$  7200 flame,  $\sigma_g$  varies over a larger range of 1.5 to 1.8  $nm$  (Fig. 13). At  $Re = 21500$  (Fig. 14),  $\sigma_g$  varies from 1.7  $nm$  near the inception region to 1.9  $nm$  near the  
610 peak- $f_v$  region. In turbulent flame, soot particles are distributed over a wider size range, even at soot inception regions. Although the soot size range increases with  $Re$ , the mode diameter in turbulent flame measures less than that of the lower  $Re$  flames. Turbulence could reduce the soot growth and aggregation owing to reduced residence time, soot precursor (PAH) concentration, and gas  
615 temperature.

### 3.4.2. Soot particle size

The axial evolution of soot mode diameter ( $D_m$ ) obtained from PSD is shown in Fig. 15 along with  $f_{v-LII}$ . For all the cases in Fig. 15, the soot size increases with a height, similar to  $f_v$ , until both reach a peak. Beyond a certain distance,  
620  $f_v$  decreases, but  $D_m$  shows a plateau until further downstream; afterward,  $D_m$  decreases with height. The reduction in  $D_m$  and  $f_v$  is due to oxidation of soot (mainly by OH) near the flame-tip region. Recall that the  $f_{v-LII}$  is time-averaged, and thus, can be affected by soot intermittency. Since  $D_m$  is the most probable value, it is less affected by soot intermittency. Conditionally averaged  
625  $f_{v-LII}$  reported in [16], confirms that the peak  $f_v$  lies further downstream than that of the time-averaged  $f_v$ . This explains the difference in axial trends of  $D_m$  and time-averaged  $f_v$ .

Since the soot particle size in turbulent  $n$ -butane flame is not yet been re-

ported in the literature, we compare the present measurements with ethylene-  
630 fueled turbulent flames and with a laminar  $n$ -butane flame. The  $D_m$  range of  
the present jet flames is close to the one interpreted from PSD reported for a  
laminar premixed  $n$ -butane flame [30]. In turbulent non-premixed ethylene jet  
flame, Gu et al. [21] reported the primary soot diameter ( $d_p$ ) based on time-  
resolved LII. The mean  $d_p$  followed a similar trend as of the mean  $f_v$  with height.  
635 The most probable  $d_p$  also showed an identical trend (and values) as of the mean  
 $d_p$  with height. The peak in  $d_p$  and  $f_v$  occurred at the same location. A similar  
trend is noted in turbulent pre-vaporized toluene flame [22]. The present mode  
(most probable) diameter evolution shows a similar trend with  $f_v$  as of [21, 22],  
within the measurement uncertainty.

640 Apart from qualitative trends, the soot particle size from ethylene flame [21]  
could be compared quantitatively with the present results while being aware  
of differences (in  $Re$ , fuel, soot size parameter). In ethylene flame [21], the  
most probable  $d_p$  varies in 8 – 16  $nm$  range. The mode diameter  $D_m$  in the  
present turbulent  $n$ -butane flame ( $Re$  21500) varies in 12 – 24  $nm$  range, which  
645 is 1.5 times of the most probable  $d_p$  with ethylene. Based on the PSD reported  
in laminar ethylene [29] and  $n$ -butane flames [30], we assume soot size in  $n$ -  
butane flames to be similar as of ethylene. Consequently, the  $D_m/d_p$  ratio of 1.5  
suggests a mild soot aggregation in the present flame. To conclude definitively,  
complementary ( $d_p$ ,  $D_m$ ,  $R_{gy}$ ,  $N_p$ , etc.) information is needed in an identical  
650 flame.

Next, we compare the present  $D_m$  trends with the mobility diameters re-  
ported by Chowdhury et al. [31]. The authors reported an axial variation of  
geometric mean diameter ( $D_g$ ) based on SMPS in diluted turbulent ethylene  
flame. Note that  $D_g$  and  $D_m$  need not be identical.  $D_g$  in the present flame  
655 is listed on respective PSD provided in Sec. 3.4.1.  $D_g$  measures consistently  
higher than  $D_m$ , typically 1.1 to 1.3 times as of  $D_m$ . The orifice blockage cor-  
rection may lead to uncertainties in  $D_g$  estimation for high sooting cases, as  
noted in Sec. 3.4.1. Recall, for  $D_g$  evaluation, data over the entire scan range  
(120  $s$  duration) is needed. Conversely,  $D_m$  evaluation requires data until peak

660 probability, which corresponds to a smaller time delay (23 s until 30 nm scan).  
 Consequently, the correction uncertainties are minimal in  $D_m$ , and therefore,  
 we chose to use  $D_m$ . The axial  $D_g$  trend in [31] shows continuous growth until  
 a certain downstream distance near the flame-tip. Beyond which measurements  
 were not available. Therefore, the peak transition from a monotonic trend could  
 665 not be identified. Additionally, the axial peak- $f_v$  location in this flame is not  
 known to assess  $f_v$  and soot size correlation. The  $D_g$  variation range in [31] is  
 rather small (3 – 6 nm) relative to the mean  $d_p$  (5 – 16 nm) reported in pure  
 ethylene flame [21]. The smaller soot size in [31] is likely due to the dilution  
 (65%  $N_2$ ) of ethylene. Decrease in  $d_p$  with  $N_2$  dilution has also been reported  
 670 by Sun et al. [59].

In the present undiluted  $n$ -butane flames, the soot size ( $D_m$ ) ranges from 12  
 to 28 nm, as observed from Fig. 15. Soot particles much smaller (2 – 4 nm)  
 than the present range have been reported [27] in low sooting laminar  $n$ -butane  
 nucleation flames. The present SMPS set-up is unable to resolve such a small size  
 675 which may occur in soot nucleation regions. In the attached flame (Fig. 15a),  
 $D_m$  measures 20 nm near the inception region, whereas in lifted flames (Figs.  
 15b and 15c) corresponding  $D_m$  is  $\sim 12$  nm. In lifted flames, partial premixing  
 is anticipated. The soot size appears to be highly sensitive to the local fuel  
 concentration. Partial premixing can reduce the fuel pyrolysis, which in turn  
 680 decreases the concentration of PAH needed for the soot growth. Nevertheless,  
 the smaller  $D_m$  in lifted flame ( $Re$  7200, Fig. 15b) grows to a peak value of  
 28 nm, which is the same as of  $Re$  5000 attached flame. At  $Re$  5000 and 7200,  
 $D_m$  rises sharply after the inception, similar to the  $f_v$  trend. In turbulent flame  
 (Fig. 15c),  $D_m$  rise trend is almost identical as of  $f_v$ . Peak  $D_m$  measures 24 nm,  
 685 which is slightly lower than  $Re$  5000 flame (28 nm). Increased  $Re$  reduces the  
 soot size marginally. With an increase in  $Re$ , the residence time and temperature  
 decrease, while air/fuel mixing enhances, which combinedly leads to lower  $D_m$ .

The effect of lift-off originated partial premixing is investigated by Grader  
 et al. [60] through LES. The impact of partial premixing is mainly relevant in  
 690 the soot inception and growth regions. In the downstream locations (between

soot growth and oxidation regions), combustion was shown to occur primarily in the non-premixed regime. This may be the reason for the substantial rise in  $D_m$  with height in lifted flames despite the upstream partial premixing.

#### 4. Conclusions

695 The present paper reports the temperature and soot particle size in  $n$ -butane jet flames. The effect of exit  $Re$  on correlations between temperature and various parameters, namely  $f_v$ , soot-precursor (PAH), and reaction zone (OH), are investigated. The soot particle size distribution was obtained at different  $Re$ . Additionally, soot concentration was measured using the *ex-situ* PPS device.

700 Time-averaged flame temperature decreases with  $Re$  due to increased flame stretch and averaging in an unsteady flame. For a given  $Re$ , the mean flame temperature decreases with height. The temperature and OH peaks are nearly aligned; however, the temperature peak is biased towards the fuel-rich side of the flame. Soot-precursor (PAH) peaks at a much lower temperature (650 K) in the  
705 attached flame ( $Re$  5000) than in the lifted flame (850 K in  $Re$  7200). In turbulent lifted flame ( $Re$  21500), peak-PAH occurs at a higher temperature (940 K). Partial premixing of air/fuel in the lifted flames can significantly increase the temperature required for PAH formation. The mean temperature at peak- $f_v$  location ( $T_{f_v^{pk}}$ ) was measured in low-sooting regions.  $T_{f_v^{pk}}$  decreases from 1400  
710 to 1200 K with height in  $Re$  5000 flame. At downstream locations, the soot growth may be facilitated by surface reactions and transported soot-precursors from upstream regions, and thus resulting in the lower  $T_{f_v^{pk}}$ . Despite the variation in turbulence level ( $Re = 5000 - 21500$ ), peak  $f_v$  at soot inception region occurs at a nearly constant value around 1400 K. The soot-temperature correlation  
715 is governed by the competition between soot formation through larger PAH and oxidation by OH near the reaction zone. These competing processes dictate the value of  $T_{f_v^{pk}}$  which is found to be less sensitive to  $Re$  in the soot inception region. To obtain further insights into the soot-temperature correlation, time-resolved (i.e., high-speed) simultaneous measurements will be beneficial

720 where one can account for a soot response delay owing to longer soot reaction timescales.

A quasi-instantaneous (averaged over 0.1 s)  $f_{v-PPS}$  deduced from the *ex-situ* PPS technique is in qualitative agreement with the *in-situ* time-averaged  $f_{v-LII}$ . However,  $f_{v-PPS}$  measures 2.4 to 2.8 times of  $f_{v-LII}$ . This difference is primarily attributed to the time-averaging of  $f_{v-LII}$  in an intermittent field. 725 If the soot intermittency is accounted for by conditional averaging of  $f_{v-LII}$ , a reasonable quantitative agreement (within  $\pm 15\%$ ) between  $f_{v-LII}$  and  $f_{v-PPS}$  is noted.

The mode diameter ( $D_m$ ) of soot particle peaks around the same axial region 730 as the peak  $f_v$ .  $D_m$  at a moderate  $Re$  (5000 or 7200) varies between 12–28 nm, whereas at  $Re$  21500 peak- $D_m$  decreases marginally to 24 nm. Turbulence can reduce the soot growth and aggregation owing to a reduced residence time, soot precursor concentration, and temperature. Although  $D_m$  decreases with  $Re$ , soot particles are distributed over a wider size range, possibly due to reduced 735 soot aggregation.  $D_m$  in turbulent flame ( $Re$  21500) measures nearly 1.5 times of the primary diameter reported in a turbulent ethylene flame [21], suggesting a moderate soot aggregation in the present flame.

In this manner, the present work examined the influence of  $Re$  on temperature-soot correlations and soot particle size. The application of the PPS device is 740 demonstrated for the first time to measure the in-flame soot concentration. Additionally, soot particle size in a turbulent *n*-butane flame is provided using SMPS. The data provided insights into the effect of upstream partial premixing and turbulence on soot size. The comprehensive database containing a wide range of parameters and boundary conditions, from the present and companion 745 (Part 1) [16] papers, can contribute towards the development and validation of turbulence and soot-chemistry models for fuels of practical relevance.

## Acknowledgments

The project (ASMAPE) was funded by the French National Research Agency (ANR) under contract no. ANR-13-TDMO-0002. Dr. I.A. Mulla acknowledges support through Marie Skłodowska-Curie Individual Fellowship (ID: 747576) awarded by the European Commission under H2020-EU.1.3.2 scheme. The assistance of Mr. F. Lefebvre in thermocouple fabrication and of Mr. B. Quevreux in component fabrication is gratefully acknowledged. The authors thank Dr. G. Lefebvre for his aid in the installation of particle analyzers. The authors also acknowledge the support of Dr. G. Godard and Mrs. C. Gobin in laser installations.

Table 1: Temperature at peak PAH radial location at different  $y$  (mm).

$Re$	$T$ (K) at peak PAH		
	$y=20$	$y=60$	$y=120$
5000	650	730	865
7200	850	875	885
21500	-	-	940

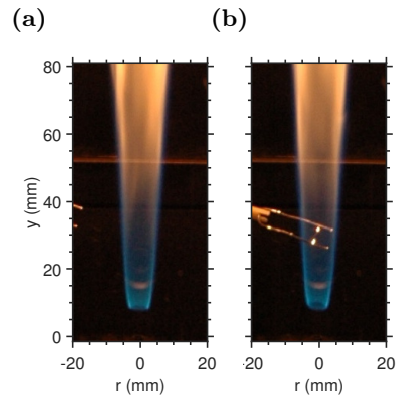


Figure 1:  $Re$  7200 flame: (a) without thermocouple, and (b) with thermocouple at  $y = 30$  mm.

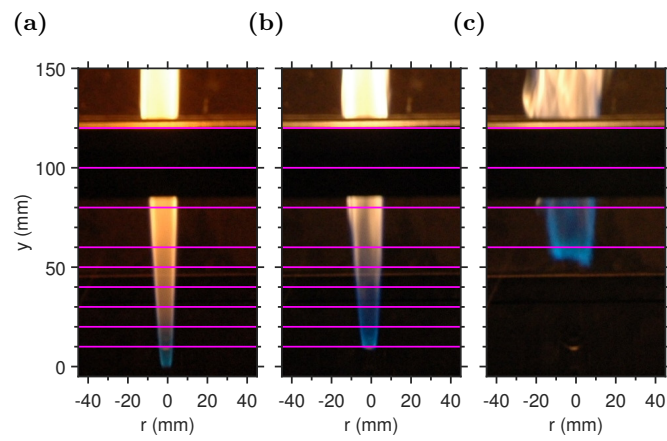


Figure 2: Flame photographs: (a)  $Re$  5000, (b)  $Re$  7200, and (c)  $Re$  21500. Temperature measurement stations are marked by magenta lines.

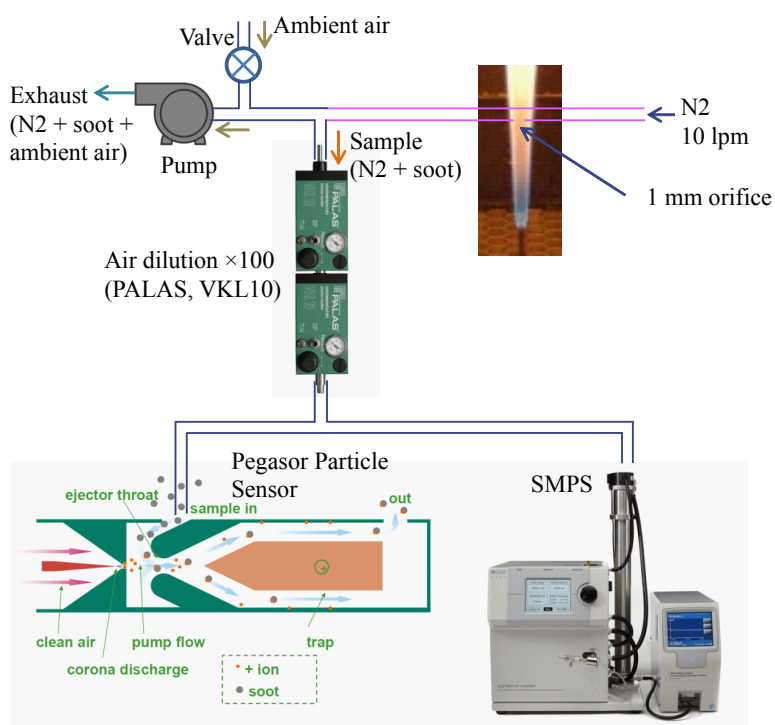


Figure 3: Probe sampling set-up for SMPS and PPS measurements.

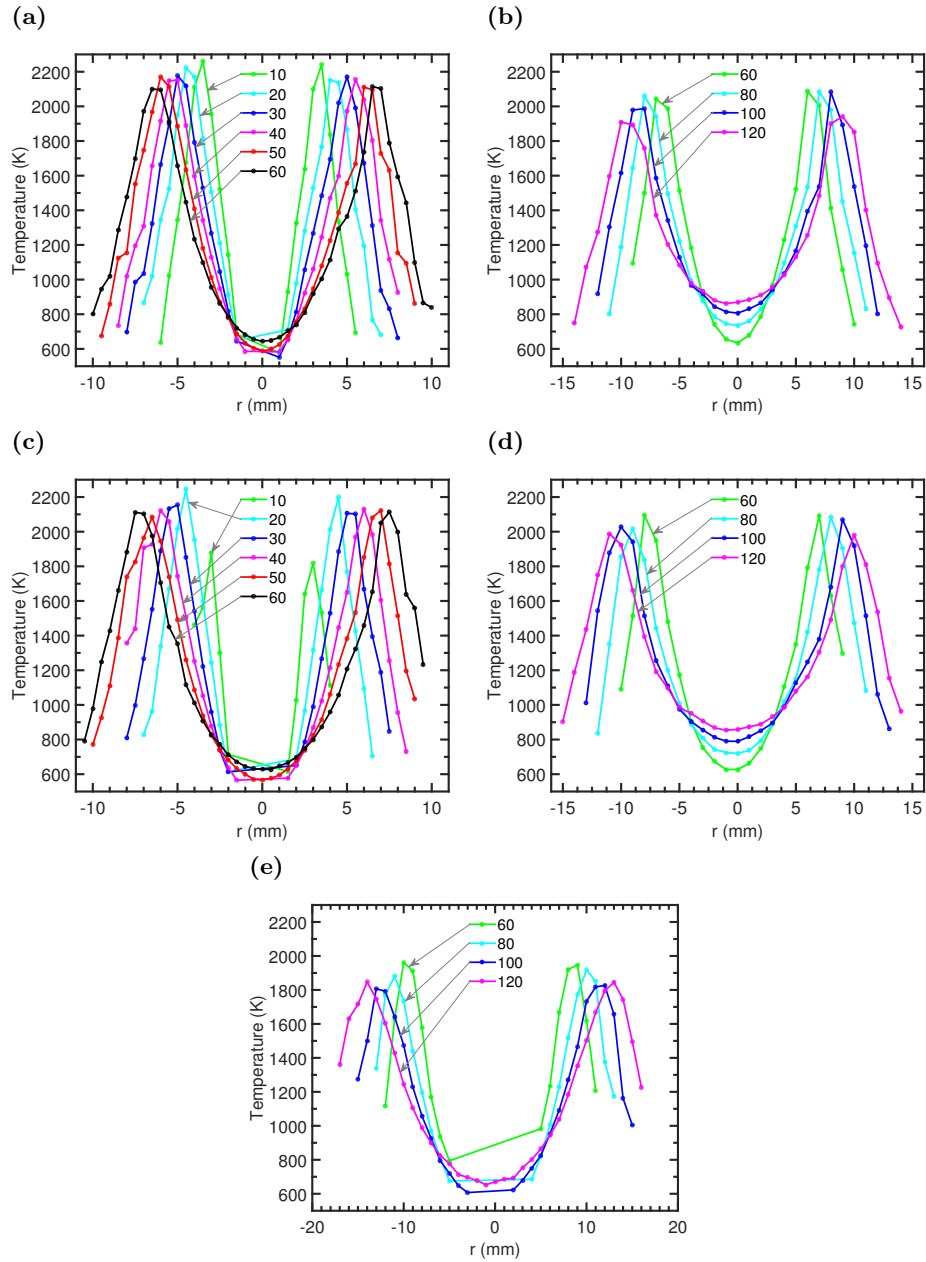


Figure 4: Mean temperature radial profiles: (a, b)  $Re$  5000, (c, d)  $Re$  7200, and (e)  $Re$  21500. The legend shows axial  $y$  stations (in  $mm$ ) as marked in Fig. 2.

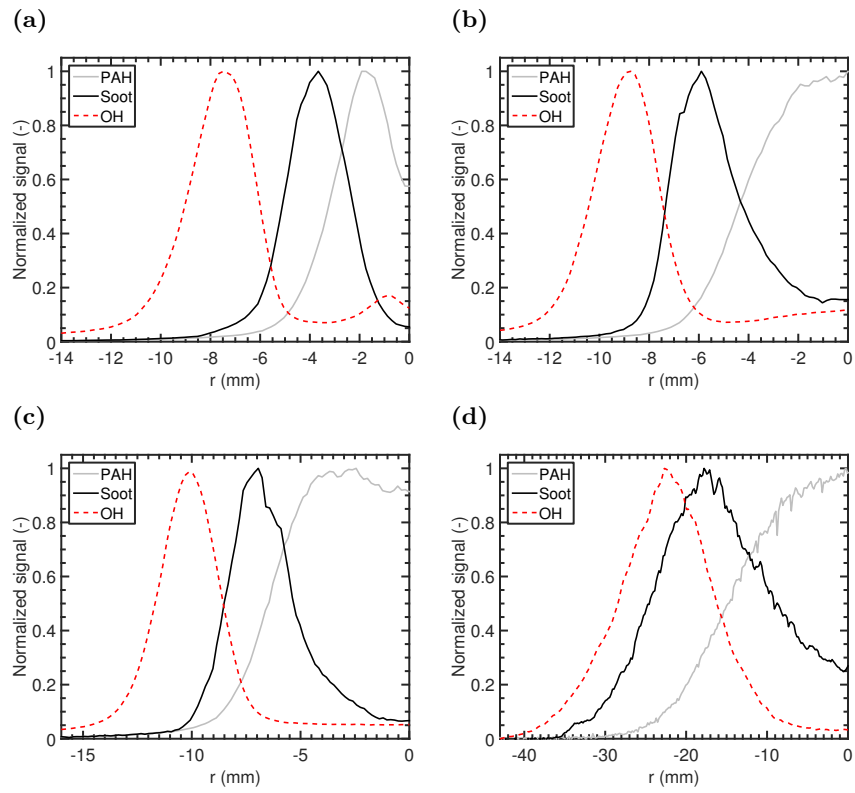


Figure 5: PAH-LIF, Soot concentration, OH-LIF mean radial profiles: (a)  $Re$  2100 at  $y = 100$  mm, (b)  $Re$  5000 at  $y = 100$  mm, (c)  $Re$  7200 at  $y = 100$  mm, and (d)  $Re$  21500 at  $y = 250$  mm. The profiles are extracted from the data reported in [16]

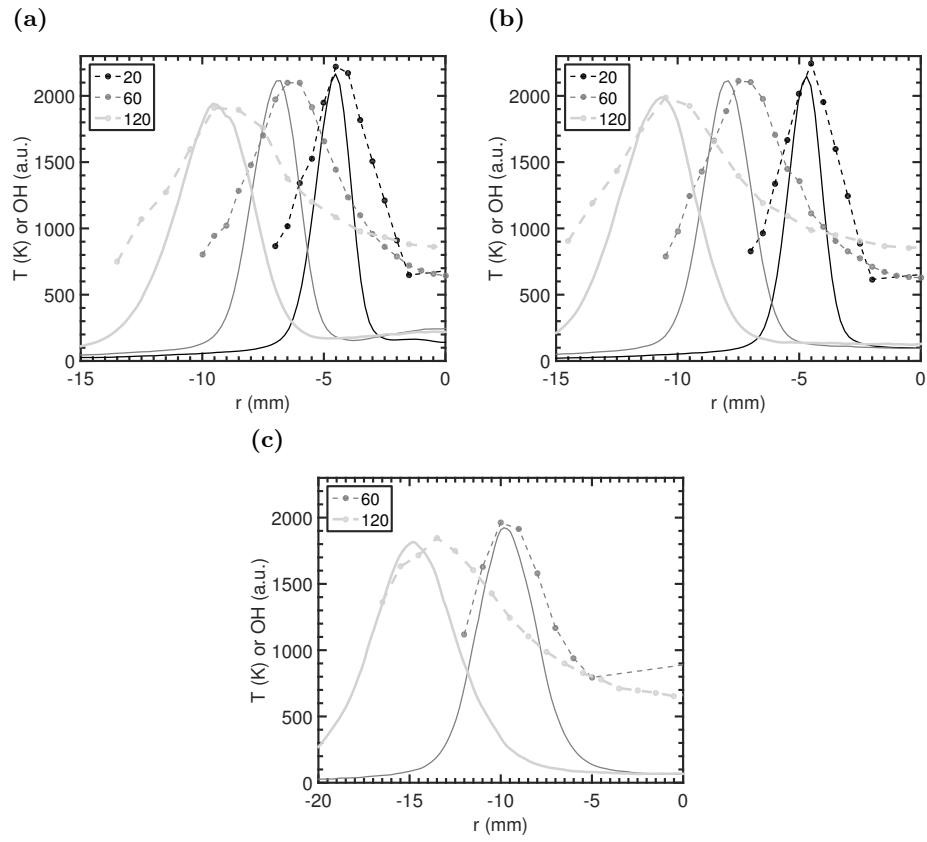


Figure 6: Temperature (dashed line) and OH-LIF (solid line) mean radial profiles: (a)  $Re$  5000, (b)  $Re$  7200, and (c)  $Re$  21500. The legend shows axial  $y$  location (in  $mm$ ).

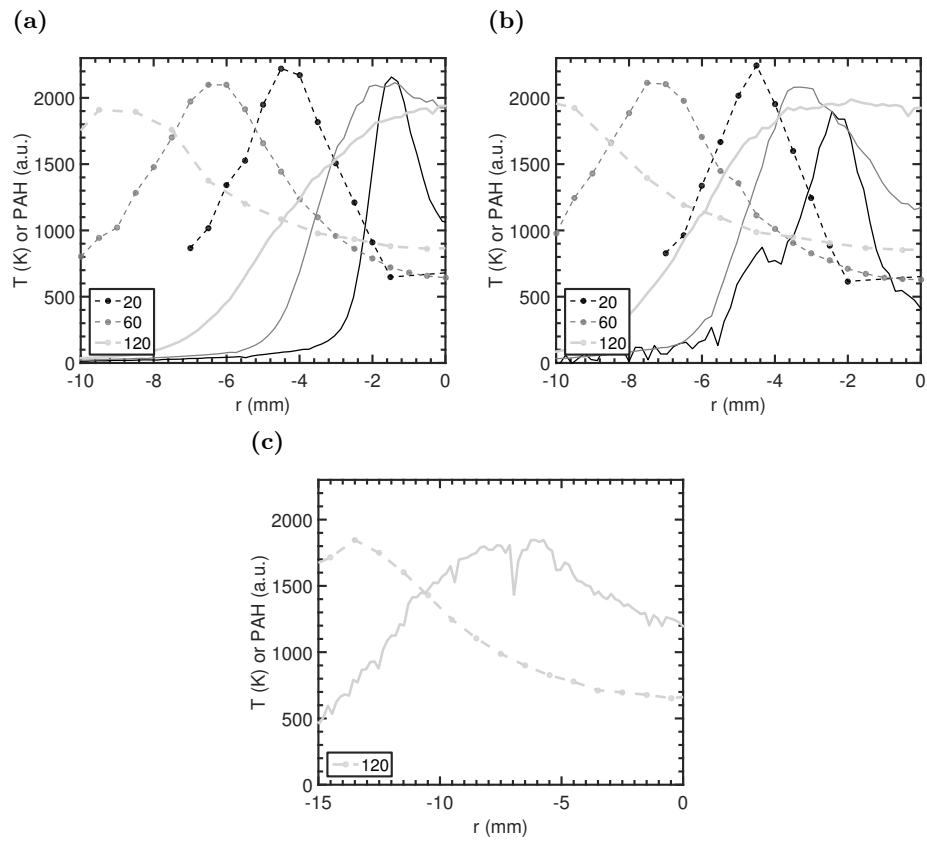


Figure 7: Temperature (dashed line) and PAH-LIF (solid line) mean radial profiles: (a)  $Re = 5000$ , (b)  $Re = 7200$ , and (c)  $Re = 21500$ . The legend shows axial  $y$  location (in  $mm$ ).

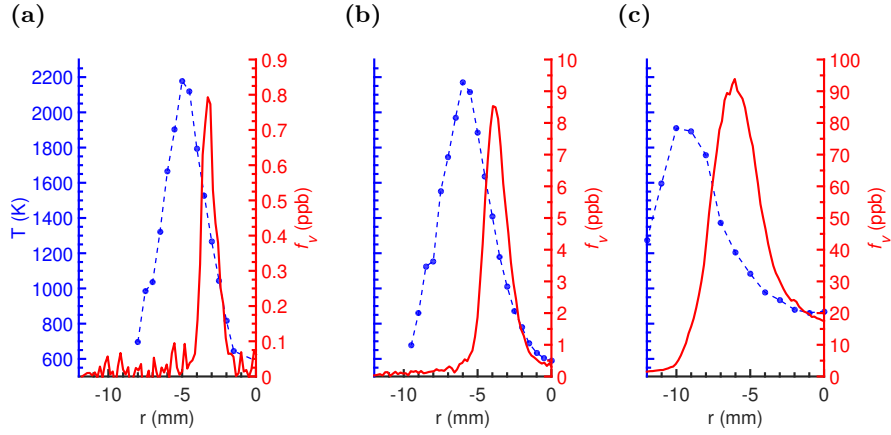


Figure 8: Temperature (dashed line) and  $f_v$  (solid line) profiles in  $Re$  7200 flame at: (a)  $y = 30$  mm, (b)  $y = 50$  mm, and (c)  $y = 120$  mm.

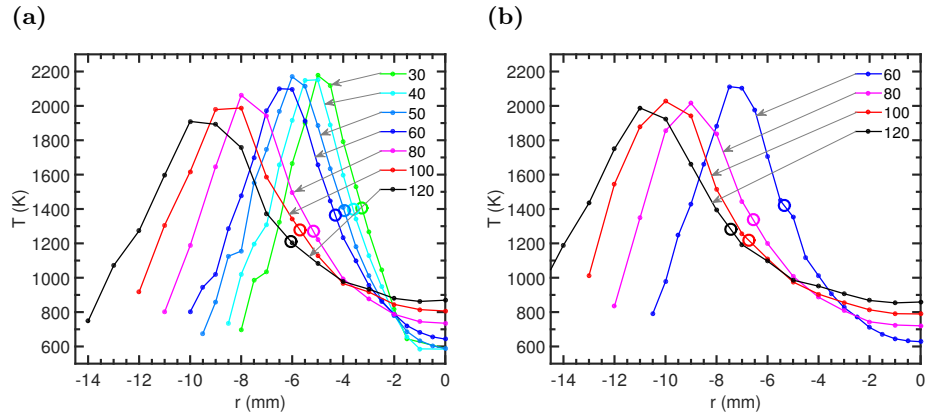


Figure 9: Temperature profiles where open circles mark the temperature at peak soot concentration location for: (a)  $Re$  5000, (b)  $Re$  7200. Axial  $y$  locations (in mm) are indicated in the legend.

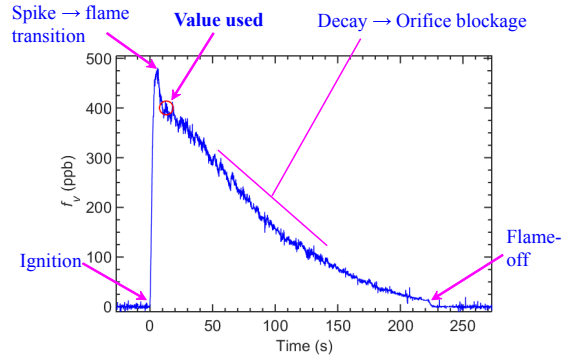


Figure 10: PPS trace in  $Re$  7200 flame at  $r = 0$  mm,  $y = 250$  mm.

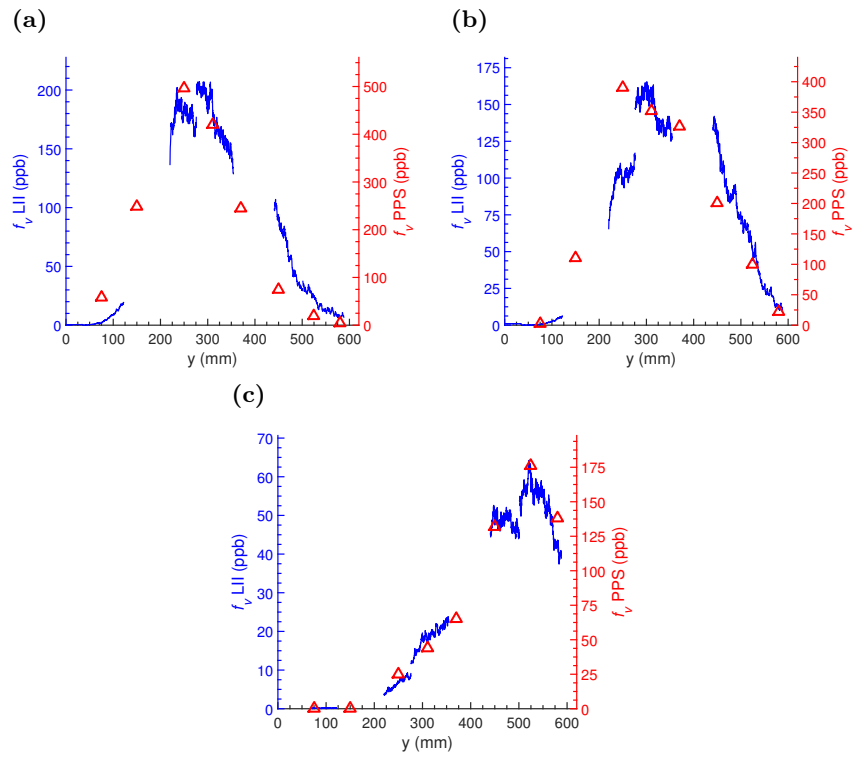


Figure 11: Axial  $f_v$  profiles from LII (line) and PPS (symbols): (a)  $Re$  5000, (b)  $Re$  7200, and (c)  $Re$  21500.

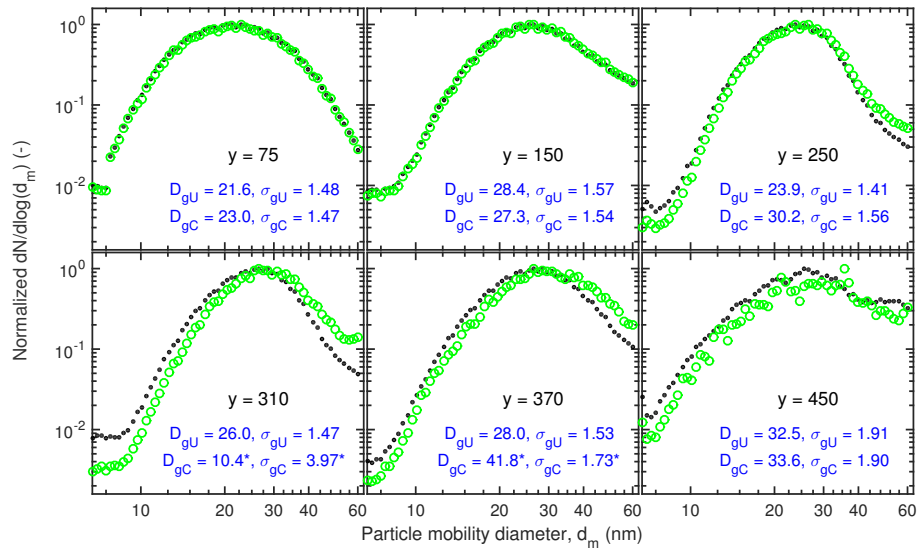


Figure 12: Soot PSDs at different heights ( $y$  in  $mm$ ) along the burner axis in  $Re$  5000 flame.  $D_g$  and  $\sigma_g$  are specified in  $nm$ . ( $\bullet$ ) without blockage correction, ( $\circ$ ) with correction.

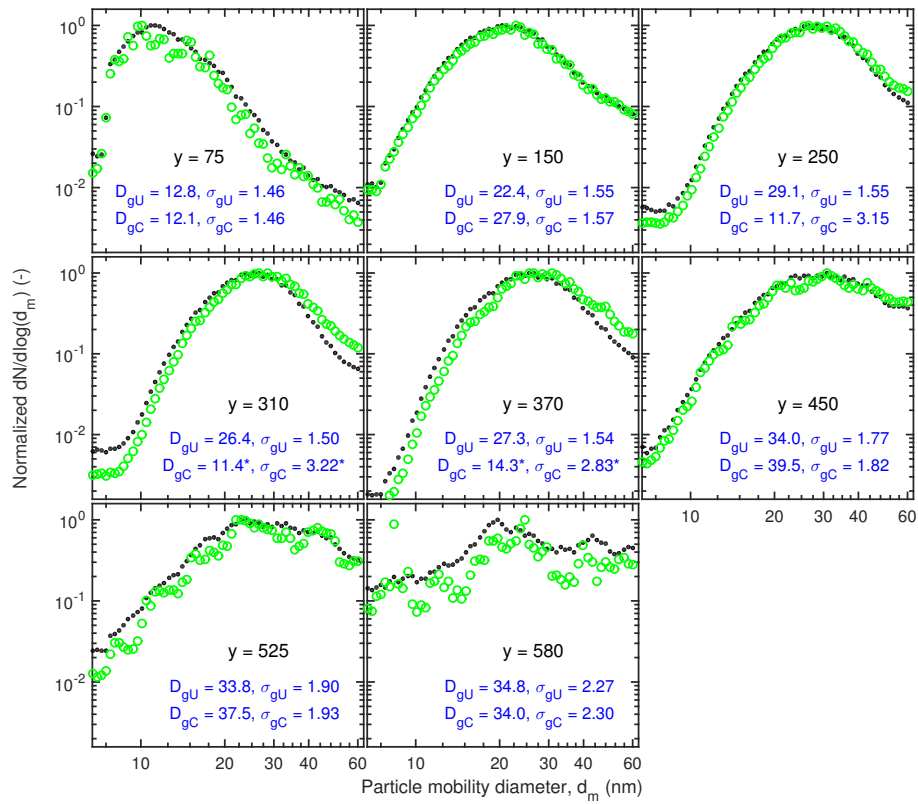


Figure 13: Soot PSDs at different heights along the burner axis in *Re* 7200 flame. (●) without blockage correction, (○) with correction.

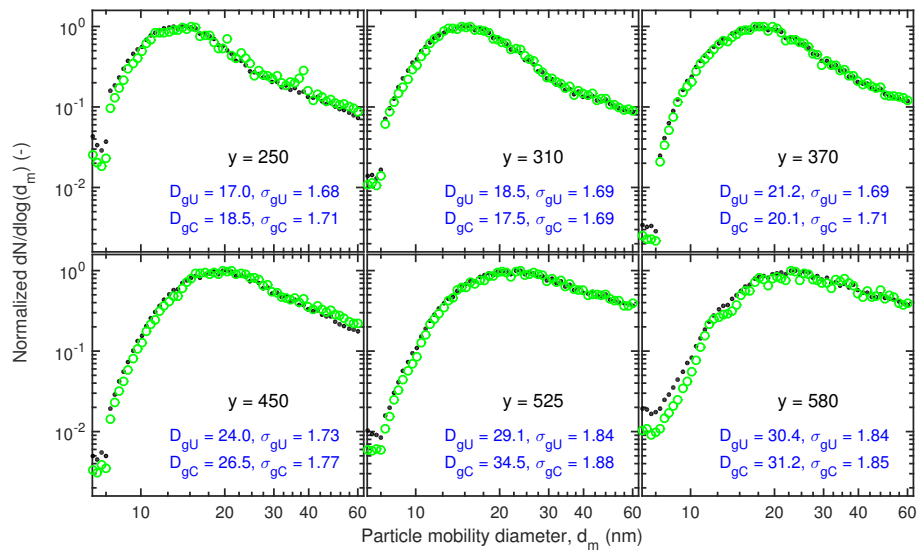


Figure 14: Soot particle size distribution at different heights along the burner axis in *Re* 21500 flame. (•) without blockage correction, (◦) with correction.

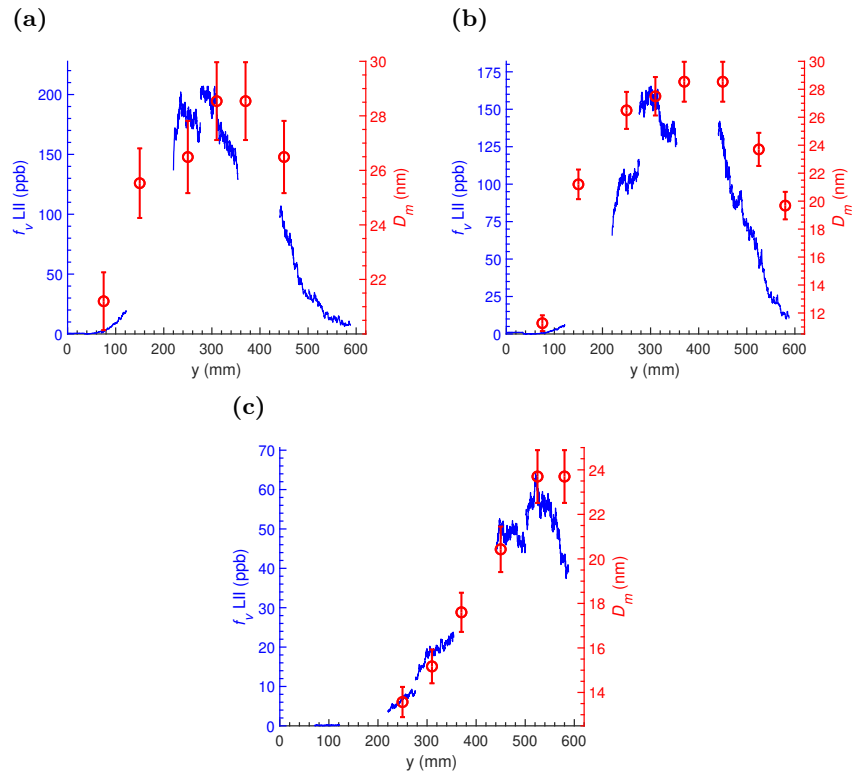


Figure 15: Soot mode diameter  $D_m$  (symbols) and  $f_v$ -LII (line) variation along the axis: (a)  $Re$  5000, (b)  $Re$  7200, and (c)  $Re$  21500.

## References

- [1] C. R. Shaddix, J. Zhang, R. W. Schefer, J. Doom, J. C. Oefelein, S. Kook, L. M. Pickett, H. Wang, Understanding and predicting soot generation in  
760 turbulent non-premixed jet flames, Sand2010-7178, Sandia Report.
- [2] M. Köhler, K. P. Geigle, W. Meier, B. M. Crosland, et al., Sooting turbulent jet flame: characterization and quantitative soot measurements, *Appl. Phys. B* 104 (2) (2011) 409–425. doi:10.1007/s00340-011-4373-y.
- [3] M. Köhler, K.-P. Geigle, T. Blacha, P. Gerlinger, W. Meier, Experimental  
765 characterization and numerical simulation of a sooting lifted turbulent jet diffusion flame, *Combust. Flame* 159 (8) (2012) 2620–2635. doi:10.1016/j.combustflame.2012.01.015.
- [4] K. P. Geigle, W. O’Loughlin, R. Hedef, W. Meier, Visualization of soot inception in turbulent pressurized flames by simultaneous measurement of  
770 laser-induced fluorescence of polycyclic aromatic hydrocarbons and laser-induced incandescence, and correlation to OH distributions, *Appl. Phys. B* 119 (4) (2015) 717–730. doi:10.1007/s00340-015-6075-3.
- [5] K. P. Geigle, R. Hedef, M. Stöhr, W. Meier, Flow field characterization of pressurized sooting swirl flames and relation to soot distributions, *Proc. Combust. Inst.* 36 (3) (2017) 3917–3924. doi:10.1016/j.proci.2016.09.024.  
775
- [6] I. E. Helou, A. W. Skiba, E. Mastorakos, Experimental investigation of soot production and oxidation in a lab-scale rich–quench–lean (RQL) burner, *Flow Turbul. Combust.* 106 (4) (2020) 1019–1041. doi:10.1007/s10494-020-00113-5.  
780
- [7] G. D. Falco, I. E. Helou, P. M. de Oliveira, M. Sirignano, R. Yuan, A. D’Anna, E. Mastorakos, Soot particle size distribution measurements in a turbulent ethylene swirl flame, *Proc. Combust. Inst.* 38 (2) (2021) 2691–2699. doi:10.1016/j.proci.2020.06.212.

- 785 [8] P. Rodrigues, B. Franzelli, R. Vicquelin, O. Gicquel, N. Darabiha, Coupling an LES approach and a soot sectional model for the study of sooting turbulent non-premixed flames, *Combust. Flame* 190 (2018) 477–499. doi:10.1016/j.combustflame.2017.12.009.
- [9] H. Koo, V. Raman, M. E. Mueller, K.-P. Geigle, LES of a sooting flame in a pressurized swirl combustor, in: 54th AIAA Aerospace Sciences Meeting, American Institute of Aeronautics and Astronautics, 2016. doi:10.2514/7.2016-2123.
- 790 [10] A. Wick, F. Priesack, H. Pitsch, Large-eddy simulation and detailed modeling of soot evolution in a model aero engine combustor, in: Volume 4A: Combustion, Fuels and Emissions, ASME, 2017. doi:10.1115/gt2017-63293.
- 795 [11] B. Franzelli, A. Vié, N. Darabiha, A three-equation model for the prediction of soot emissions in LES of gas turbines, *Proc. Combust. Inst.* 37 (4) (2019) 5411–5419. doi:10.1016/j.proci.2018.05.061.
- 800 [12] S. Gkantonas, M. Sirignano, A. Giusti, A. D’Anna, E. Mastorakos, Comprehensive soot particle size distribution modelling of a model rich-quench-lean burner, *Fuel* 270 (2020) 117483. doi:10.1016/j.fuel.2020.117483.
- [13] N. M. Marinov, W. J. Pitz, C. K. Westbrook, A. M. Vincitore, M. J. Castaldi, S. M. Senkan, C. F. Melius, Aromatic and polycyclic aromatic hydrocarbon formation in a laminar premixed n-butane flame, *Combust. Flame* 114 (1-2) (1998) 192–213. doi:10.1016/s0010-2180(97)00275-7.
- 805 [14] W. J. Pitz, C. K. Westbrook, Chemical kinetics of the high pressure oxidation of n-butane and its relation to engine knock, *Combust. Flame* 63 (1-2) (1986) 113–133. doi:10.1016/0010-2180(86)90115-x.
- 810 [15] Y. Huang, C. Sung, J. Eng, Dilution limits of n-butane/air mixtures under conditions relevant to HCCI combustion, *Combust. Flame* 136 (4) (2004) 457–466. doi:10.1016/j.combustflame.2003.10.011.

- [16] I. Mulla, B. Lecordier, P. Desgroux, A. Cessou, Comprehensive characterization of sooting butane jet flames, Part 1: soot, soot-precursor, and reaction zone, *Combust. Flame* CNF-D-18-00805R1 (2021) Accepted. 815
- [17] A. Coppalle, D. Joyeux, Temperature and soot volume fraction in turbulent diffusion flames: Measurements of mean and fluctuating values, *Combust. Flame* 96 (3) (1994) 275–285. doi:10.1016/0010-2180(94)90014-0.
- [18] C. R. Shaddix, J. Zhang, Joint temperature-volume fraction statistics of soot in turbulent non-premixed jet flames, in: 8th U.S. National Combustion Meeting, 2013, p. paper 2E11. 820
- [19] Q. N. Chan, P. R. Medwell, P. A. Kalt, Z. T. Alwahabi, et al., Simultaneous imaging of temperature and soot volume fraction, *Proc. Combust. Inst.* 33 (1) (2011) 791–798. doi:10.1016/j.proci.2010.06.031.
- [20] S. Mahmoud, G. Nathan, P. Medwell, B. Dally, Z. Alwahabi, Simultaneous planar measurements of temperature and soot volume fraction in a turbulent non-premixed jet flame, *Proc. Combust. Inst.* 35 (2) (2015) 1931–1938. doi:10.1016/j.proci.2014.06.122. 825
- [21] D. Gu, Z. Sun, B. B. Dally, P. R. Medwell, et al., Simultaneous measurements of gas temperature, soot volume fraction and primary particle diameter in a sooting lifted turbulent ethylene/air non-premixed flame, *Combust. Flame* 179 (2017) 33–50. doi:10.1016/j.combustflame.2017.01.017. 830
- [22] S. Kruse, J. Ye, Z. Sun, A. Attili, et al., Experimental investigation of soot evolution in a turbulent non-premixed prevaporized toluene flame, *Proc. Combust. Inst.* 37 (1) (2019) 849–857. doi:10.1016/j.proci.2018.05.075. 835
- [23] O. Park, R. A. Burns, O. R. Buxton, N. T. Clemens, Mixture fraction, soot volume fraction, and velocity imaging in the soot-inception region of a turbulent non-premixed jet flame, *Proc. Combust. Inst.* 36 (1) (2017) 899–907. doi:10.1016/j.proci.2016.08.048. 840

- [24] O. Park, R. A. Burns, N. T. Clemens, Relationship between soot and scalar dissipation rate in the soot-inception region of turbulent non-premixed jet flames, *Proc. Combust. Inst.* 37 (1) (2019) 1057–1064. doi:10.1016/j.proci.2018.06.174.
- 845 [25] J. Reimann, S.-A. Kuhlmann, S. Will, 2D aggregate sizing by combining laser-induced incandescence (LII) and elastic light scattering (ELS), *Appl. Phys. B* 96 (4) (2009) 583–592. doi:10.1007/s00340-009-3546-4.
- [26] C. Gu, H. Lin, J. Camacho, B. Lin, C. Shao, et al., Particle size distribution of nascent soot in lightly and heavily sooting premixed ethylene flames, 850 *Combust. Flame* 165 (2016) 177–187. doi:10.1016/j.combustflame.2015.12.002.
- [27] C. Betrancourt, F. Liu, P. Desgroux, X. Mercier, et al., Investigation of the size of the incandescent incipient soot particles in premixed sooting and nucleation flames of n-butane using LII, HIM, and 1 nm-SMPS, *Aerosol Sci. Technol.* 51 (8) (2017) 916–935. doi:10.1080/02786826.2017.1325440. 855
- [28] B. Zhao, Z. Yang, M. V. Johnston, H. Wang, et al., Measurement and numerical simulation of soot particle size distribution functions in a laminar premixed ethylene-oxygen-argon flame, *Combust. Flame* 133 (1-2) (2003) 173–188. doi:10.1016/s0010-2180(02)00574-6.
- 860 [29] A. D. Abid, N. Heinz, E. D. Tolmachoff, D. J. Phares, et al., On evolution of particle size distribution functions of incipient soot in premixed ethylene-oxygen-argon flames, *Combust. Flame* 154 (4) (2008) 775–788. doi:10.1016/j.combustflame.2008.06.009.
- [30] J. Camacho, S. Lieb, H. Wang, Evolution of size distribution of nascent soot 865 in n- and i-butanol flames, *Proc. Combust. Inst.* 34 (1) (2013) 1853–1860. doi:10.1016/j.proci.2012.05.100.
- [31] S. Chowdhury, W. R. Boyette, W. L. Roberts, Time-averaged probability density functions of soot nanoparticles along the centerline of a piloted

- turbulent diffusion flame using a scanning mobility particle sizer, *J. Aerosol Sci.* 106 (2017) 56–67. doi:10.1016/j.jaerosci.2016.10.012.
- 870 [32] W. Boyette, S. Chowdhury, W. Roberts, Soot particle size distribution functions in a turbulent non-premixed ethylene-nitrogen flame, *Flow Turbul. Combust.* 98 (4) (2017) 1173–1186. doi:10.1007/s10494-017-9802-5.
- [33] J. Jang, Y.-J. Lee, O. Kwon, M. Lee, J. Kim, The effect of engine oil  
875 on particulate matter, emissions and fuel economy in gasoline and diesel vehicle, in: *SAE Technical Paper Series*, SAE International, 2014. doi:10.4271/2014-01-2837.
- [34] L. Tarabet, K. Loubar, M. Lounici, K. Khiari, et al., Experimental investigation of DI diesel engine operating with eucalyptus biodiesel/natural gas  
880 under dual fuel mode, *Fuel* 133 (2014) 129–138. doi:10.1016/j.fuel.2014.05.008.
- [35] S. Amanatidis, M. M. Maricq, L. Ntziachristos, Z. Samaras, Measuring number, mass, and size of exhaust particles with diffusion chargers: The dual pegasor particle sensor, *J. Aerosol Sci.* 92 (2016) 1–15. doi:10.1016/j.jaerosci.2015.10.005.
- 885 [36] R. C. Deo, J. Mi, G. J. Nathan, The influence of reynolds number on a plane jet, *Phys. Fluids* 20 (7) (2008) 075108. doi:10.1063/1.2959171.
- [37] Z. W. Sun, Z. T. Alwahabi, D. H. Gu, S. M. Mahmoud, et al., Planar laser-induced incandescence of turbulent sooting flames: the influence of  
890 beam steering and signal trapping, *Appl. Phys. B* 119 (4) (2015) 731–743. doi:10.1007/s00340-015-6080-6.
- [38] S.-Y. Lee, S. R. Turns, R. J. Santoro, Measurements of soot, OH, and PAH concentrations in turbulent ethylene/air jet flames, *Combust. Flame* 156 (12) (2009) 2264–2275. doi:10.1016/j.combustflame.2009.09.005.
- 895 [39] V. Narayanaswamy, N. Clemens, Simultaneous LII and PIV measurements in the soot formation region of turbulent non-premixed jet flames, *Proc.*

- Combust. Inst. 34 (1) (2013) 1455–1463. [doi:10.1016/j.proci.2012.06.018](https://doi.org/10.1016/j.proci.2012.06.018).
- [40] S. Mahmoud, G. Nathan, Z. Alwahabi, Z. Sun, P. Medwell, B. Dally, The  
900 effect of exit reynolds number on soot volume fraction in turbulent non-  
premixed jet flames, Combust. Flame 187 (2018) 42–51. [doi:10.1016/j.combustflame.2017.08.020](https://doi.org/10.1016/j.combustflame.2017.08.020).
- [41] B. Franzelli, P. Scouffaire, S. Candel, Time-resolved spatial patterns and  
interactions of soot, PAH and OH in a turbulent diffusion flame, Proc.  
905 Combust. Inst. 35 (2) (2015) 1921–1929. [doi:10.1016/j.proci.2014.06.123](https://doi.org/10.1016/j.proci.2014.06.123).
- [42] S. Bejaoui, X. Mercier, P. Desgroux, E. Therssen, Laser induced fluo-  
rescence spectroscopy of aromatic species produced in atmospheric soot-  
ing flames using UV and visible excitation wavelengths, Combust. Flame  
910 161 (10) (2014) 2479–2491. [doi:10.1016/j.combustflame.2014.03.014](https://doi.org/10.1016/j.combustflame.2014.03.014).
- [43] C. S. McEnally, U. O. Köylü, L. D. Pfefferle, D. E. Rosner, Soot volume  
fraction and temperature measurements in laminar nonpremixed flames  
using thermocouples, Combust. Flame 109 (4) (1997) 701–720. [doi:10.1016/s0010-2180\(97\)00054-0](https://doi.org/10.1016/s0010-2180(97)00054-0).
- 915 [44] B. Zhao, Z. Yang, J. Wang, M. V. Johnston, H. Wang, Analysis of soot  
nanoparticles in a laminar premixed ethylene flame by scanning mobility  
particle sizer, Aerosol Sci. Technol. 37 (8) (2003) 611–620. [doi:10.1080/02786820300908](https://doi.org/10.1080/02786820300908).
- [45] L. Ntziachristos, S. Amanatidis, Z. Samaras, K. Janka, J. Tikkanen, Ap-  
920 plication of the pegasor particle sensor for the measurement of mass and  
particle number emissions, SAE Int. J. Fuels Lubr. 6 (2) (2013) 521–531.  
[doi:10.4271/2013-01-1561](https://doi.org/10.4271/2013-01-1561).
- [46] F. Liu, K. Daun, D. Snelling, G. Smallwood, Heat conduction from a spher-  
ical nano-particle: status of modeling heat conduction in laser-induced

- 925 incandescence, *Appl. Phys. B* 83 (3) (2006) 355–382. doi:10.1007/s00340-006-2194-1.
- [47] F. Liu, H. Guo, G. J. Smallwood, O. L. Gülder, Effects of gas and soot radiation on soot formation in a coflow laminar ethylene diffusion flame, *J. Quant. Spectrosc. Radiat. Transfer* 73 (2-5) (2002) 409–421. doi:10.1016/s0022-4073(01)00205-9.
- 930 [48] H. Nakamura, R. Tanimoto, T. Tezuka, S. Hasegawa, K. Maruta, Soot formation characteristics and PAH formation process in a micro flow reactor with a controlled temperature profile, *Combust. Flame* 161 (2) (2014) 582–591. doi:10.1016/j.combustflame.2013.09.004.
- 935 [49] A. D’Anna, M. Commodo, M. Sirignano, P. Minutolo, R. Pagliara, Particle formation in opposed-flow diffusion flames of ethylene: An experimental and numerical study, *Proc. Combust. Inst.* 32 (1) (2009) 793–801. doi:10.1016/j.proci.2008.06.200.
- [50] H. Guo, P. M. Anderson, P. B. Sunderland, Optimized rate expressions for soot oxidation by OH and O<sub>2</sub>, *Fuel* 172 (2016) 248–252. doi:10.1016/j.fuel.2016.01.030.
- 940 [51] A. Kronenburg, R. Bilger, J. Kent, Modeling soot formation in turbulent methane–air jet diffusion flames, *Combust. Flame* 121 (1-2) (2000) 24–40. doi:10.1016/s0010-2180(99)00146-7.
- 945 [52] J. M. Donbar, J. F. Driscoll, C. D. Carter, Reaction zone structure in turbulent nonpremixed jet flames—from CH-OH PLIF images, *Combust. Flame* 122 (1-2) (2000) 1–19. doi:10.1016/s0010-2180(00)00098-5.
- [53] S. Turns, *An introduction to combustion: Concepts and Applications*, 3rd Ed., McGraw-Hill, 2012.
- 950 [54] M. Stöhr, K. Geigle, R. Hadeff, I. Boxx, C. Carter, M. Grader, P. Gerlinger, Time-resolved study of transient soot formation in an aero-engine model

combustor at elevated pressure, *Proc. Combust. Inst.* 37 (4) (2019) 5421–5428. [doi:10.1016/j.proci.2018.05.122](https://doi.org/10.1016/j.proci.2018.05.122).

955 [55] F. Bisetti, G. Blanquart, M. E. Mueller, H. Pitsch, On the formation and early evolution of soot in turbulent nonpremixed flames, *Combust. Flame* 159 (1) (2012) 317–335. [doi:10.1016/j.combustflame.2011.05.021](https://doi.org/10.1016/j.combustflame.2011.05.021).

[56] B. M. Crosland, K. A. Thomson, M. R. Johnson, Simultaneous instantaneous measurements of soot volume fraction, primary particle diameter, and aggregate size in turbulent buoyant diffusion flames, *Proc. Combust. Inst.* 35 (2) (2015) 1851–1859. [doi:10.1016/j.proci.2014.06.003](https://doi.org/10.1016/j.proci.2014.06.003).  
960

[57] T. Williams, C. Shaddix, K. Jensen, J. Suo-Anttila, Measurement of the dimensionless extinction coefficient of soot within laminar diffusion flames, *Int. J. Heat Mass Transfer* 50 (7-8) (2007) 1616–1630. [doi:10.1016/j.ijheatmasstransfer.2006.08.024](https://doi.org/10.1016/j.ijheatmasstransfer.2006.08.024).

965 [58] L. Ntziachristos, P. Fragkiadoulakis, Z. Samaras, K. Janka, J. Tikkanen, Exhaust particle sensor for OBD application, in: SAE Technical Paper Series, SAE International, 2011. [doi:10.4271/2011-01-0626](https://doi.org/10.4271/2011-01-0626).

[59] Z. Sun, B. Dally, G. Nathan, Z. Alwahabi, Effects of hydrogen and nitrogen on soot volume fraction, primary particle diameter and temperature in laminar ethylene/air diffusion flames, *Combust. Flame* 175 (2017) 270–282.  
970 [doi:10.1016/j.combustflame.2016.08.031](https://doi.org/10.1016/j.combustflame.2016.08.031).

[60] M. Grader, C. Eberle, P. Gerlinger, Large-eddy simulation and analysis of a sooting lifted turbulent jet flame, *Combust. Flame* 215 (2020) 458–470. [doi:10.1016/j.combustflame.2020.01.042](https://doi.org/10.1016/j.combustflame.2020.01.042).